Electronic Supplementary Material (ESI) for Nanoscale.
This journal is © The Royal Society of Chemistry 2020

Supporting Information for

Tailoring molecular interactions between microporous polymers in high-performance mixed matrix membranes for gas separations

Cher Hon Lau,*[,a] Kristina Konstas,[b] Cara M. Doherty,[b] Stefan J. D. Smith,[b] Rujing Hou,[b,c] Huanting Wang, [c] Mariolino Carta,[d] Heewook Yoon,[e] Jaesung Park,[e] Benny D. Freeman,[e] Richard Malpass-Evans,[f] Elsa Lasseuguette,[a] Maria-Chiara Ferrari,[a] Neil B. McKeown,*[,f] Matthew R. Hill *[,b,c]

[a] School of Engineering, University of Edinburgh, Robert Stevenson Road, Edinburgh EH9 3FB, UK
[b] CSIRO, Bag 10, Clayton South, VIC 3169, Australia
[c] Department of Chemical Engineering, Monash University, Clayton, VIC 3169, Australia.
[d] Department of Chemistry, College of Science, Grove Building, Singleton Park, Swansea University, Swansea (UK), SA2 8PP
[e] Department of Chemical Engineering, University of Texas, Austin, TX78758
[f] EastChem, School of Chemistry, University of Edinburgh, David Brewster Road, Edinburgh EH9 3FJ, UK

Table of Contents

S1. Synthesis and characterisation of PIM-EA(H_2)-TB

Commercially available reagents were used without further purification. Anhydrous dichloromethane was obtained by distillation over calcium hydride under nitrogen atmosphere. Anhydrous *N*,*N*-dimethylformamide was bought from Aldrich. All reactions using air/moisture sensitive reagents were performed in oven-dried or flame-dried apparatus, under a nitrogen atmosphere.

TLC analysis refers to analytical thin layer chromatography, using aluminium-backed plates coated with Merck Kieselgel 60 GF_{254}. Product spots were viewed either by the quenching of UV fluorescence, or by staining with a solution of Cerium Sulfate in aqueous H2SO4.

Flash chromatography was performed on silica gel 60A (35-70 micron) chromatography grade (Fisher Scientific). Microwaved irradiation synthesis was performed with a CEM Discover microwave reactor. Melting points were recorded using a Gallenkamp Melting Point Apparatus and are uncorrected.

^{1}H NMR spectra were recorded in the solvent stated using an Avance Bruker DPX 400 (400 MHz) or DPX 500 (500 MHz) instruments, with ^{13}C NMR spectra recorded at 100 MHz or 125 MHz respectively.

Low-resolution mass spectrometric data were determined using a Fisons VG Platform II quadrupole instrument using electron impact ionization (EI) unless otherwise stated. High-resolution mass spectrometric data were obtained in electron impact ionization (EI) mode unless otherwise reported, on a Waters Q-TOF micromass spectrometer.

The TGA was performed using the device Thermal Analysis SDT Q600 at a heating rate of 10 °C/min from room temperature to 1000 °C.

Viscosity measurement were carried out with an Ubbelhode capillary (Nr 532 00/0, Schott Germany) on a SCHOTT Instruments GmbH: AVS 370, maintaining 25 °C, using $CHCl_3$ as solvent with 0.0013 g cm^{-3} concentration.

S2. Synthesis of PIM-EA(H_2)-TB

9,10-dihydro-11,12-*cis*(*trans*)dichloro-9,10-ethanoanthracene[1] (1)

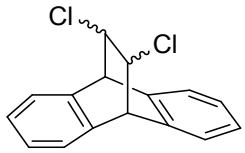

A mixture of *cis*/*trans* (1:1) 1,2-dichloroethylene (3.80 g, 39.1 mmol) and anthracene (2.00 g, 11.2 mmol) were heated to 215 ºC at 200 PSI for 5 h under microwave irradiation (300 W fixed). Excess 1,2-dichloroethylene was removed under vacuum and the black residue was dissolved in toluene (50 ml). Furan-2,5-dione (maleic anhydride) (1.00 g, 10 mmol) was added and the mixture was refluxed for 16 h to remove residual anthracene. The mixture was cooled to room temperature and the solvent was removed under vacuum. The black residue subjected to column chromatography (*n*-hexane) and the resulting yellow crystals were recrystallised from ethanol to afford the desired product 9,10-dihydro-11,12-*cis*(*trans*)dichloro-9,10-ethanoanthracene as colourless crystals(1.54 g, 50%). Mp: 190-192 ºC (Lit[1] *cis*: 203-204 ºC, *trans*: 113-114 ºC); ^{1}H NMR (500 MHz, $CDCl_3$) δ 7.44 (m, 2H), 7.37 (m, 2H), 7.30 (m, 2H), 7.23 (m, 2H), 4.57 (s, 2H), 4.52 (s, 2H); ^{13}C NMR (125 MHz, $CDCl_3$) δ 140.3, 137.9, 127.8, 127.4, 127.2, 126.8, 126.5, 125.2, 1124.6, 58.7, 52.6, 48.0, 45.4; TOF-HRMS (EI, m\z): calculated $C_{16}H_{12}Cl_2$ 274.0316 found: 274.0313 [M^+].

9,10-dihydro-9,10-ethenoanthracene (Dibenzobarrelene)[1] (2)

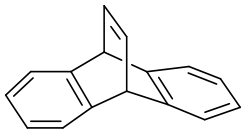

Under a nitrogen atmosphere, 9,10-dihydro-11,12-*cis*(*trans*)dichloro-9,10-ethanoanthracene (5) (6.60 g, 24 mmol) was dissolved in a refluxing mixture of anhydrous tetrahydrofuran (100 ml) and anhydrous propan-2-ol (100 ml). Sodium metal (5.49 g, 240 mmol) was added slowly in small portions and the mixture was refluxed until the sodium had been consumed. The mixture was cooled to room temperature and quenched in water. The white precipitate was filtered, washed with water and dried. The precipitate was recrystallised from methanol to afford the desired product 9,10-dihydro-9,10-ethenoanthracene as colourless crystals(3.50 g, 71%). Mp: 125-126ºC (Lit[1] 118-119 ºC); ^{1}H NMR (500 MHz, $CDCl_3$) δ 7.39 (m, 4H), 7.11 (m, 2H), 7.06 (m, 4H), 5.25 (m, 2H); ^{13}C NMR (125 MHz, $CDCl_3$) δ 146.2, 139.5, 124.552, 123.1, 51.3; TOF-HRMS (EI, m\z): calculated $C_{16}H_{12}$ 204.0939 found: 204.0943 [M^+].

9,10-dihydro-9,10-ethanoanthracene[1] (3)

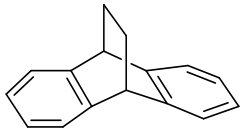

Under a nitrogen atmosphere, 9,10-dihydro-9,10-ethenoanthracene (6) (5.00 g, 24 mmol) was dissolved in tetrahydrofuran (100 ml, de-oxygenated). Raney nickel (~40 mg) and hydrazine monohydrate (24.7 ml, 24.50 g, 490 mmol) was added and the mixture was refluxed for 24 h. The colourless mixture was cooled to room temperature and filtered under nitrogen. The organic phase was extracted with chloroform and the solvent was removed under vacuum at to afford the desired product 9,10-dihydro-9,10-ethanoanthracene in a quantitative yield as

colourless crystals. Mp: 143-144 ºC (Lit[1] 142-143 ºC); ^{1}H NMR (500 MHz, $CDCl_3$) δ 7.17 (m, 4H), 7.00 (m, 4H), 4.23 (s, 2H), 1.61 (m, 4H); ^{13}C NMR (125 MHz, $CDCl_3$) δ143.9, 125.6, 123.4, 44.1, 26.8; TOF-HRMS (EI, m\z): calculated $C_{16}H_{14}$ 206.1096 found: 206.1096 [M^+].

9,10-dihydro-2,6(7)-dinitro-9,10-ethanoanthracene (4)

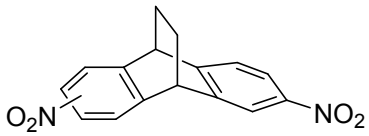

Trifluoroacetic anhydride (40.50 ml, 61.18 g, 290 mmol) was added drop-wise to a mixture of potassium nitrate ((19.61 g, 194 mmol) and 9,10-dihydro-9,10-ethanoanthracene (20 g, 97 mmol) in acetonitrile (400 ml). The mixture was stirred for 24 h, after which time a white precipitate had formed. The solvent was removed under vacuum and the residue was stirred in water then extracted with chloroform to afford a yellow solid. The crude product was subjected to column chromatography (eluent: chloroform) to afford the desired product (28.43 g, 99%) as an off-white powder. Mp: 132-133 ºC; ^{1}H NMR (500 MHz, $CDCl_3$) δ 8.18 (m, 2H), 8.08 (m, 1H), 8.06 (m, 1H), 7.49 (d, *J* = 8.10 Hz, 1H), 7.47 (d, *J* = 8.10 Hz, 1H), 4.64 (s, 2H), 1.82 (s, 4H); ^{13}C NMR (125 MHz, $CDCl_3$) δ 149.8, 149.3, 146.4, 143.9, 143.4, 124.5, 124.4, 122.1, 118.9, 118.8, 44.1, 44.0, 43.9, 25.6, 25.6, 25.5; TOF-HRMS (EI, m\z): calculated $C_{16}H_{12}N_2O_4$ 296.0797 found: 296.0800 [M^+].

9,10-dihydro-2,6(7)-diamino-9,10-ethanoanthracene (EA(H_2)-NH_2)

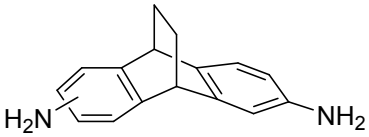

Under a nitrogen atmosphere, 9,10-dihydro-2,6(7)-dinitro-9,10-ethanoanthracene (5.00 g, 17 mmol) was suspended in diethyl ether (de-oxygenated, 200 ml). Raney nickel (~40 mg) and hydrazine monohydrate (18.90 g, 34 mmol) was added and the mixture was refluxed for 24 h. The colourless mixture was cooled in ice and filtered under nitrogen. The organic phase was extracted with diethyl ether and the solvent was removed under vacuum at 25 ºC to afford the desired product 9,10-dihydro-2,6(7)-diamino-9,10-ethanoanthracene as a colourless powder in a quantitative yield. Mp: 181-185 ºC; ^{1}H NMR (500 MHz, $CDCl_3$) δ 7.01 (d, *J* = 7.74 Hz, 1H), 7.00 (d, *J* = 7.74 Hz, 1H), 6.64 (m, 2H), 6.41 (m, 2H), 4.10 (m, 2H), 3.48 (s, br, 4H), 1.68 (s, 4H); ^{13}C NMR (125 MHz, $CDCl_3$) δ 145.8, 144.9, 144.1, 144.0, 135.3, 134.2, 123.8, 123.5, 111.8, 111.6, 111.2, 110.9, 44.4, 43.4, 42.3, 27.7, 27.2, 26.7; TOF-HRMS (EI, m\z): calculated $C_{16}H_{16}N_2$ 236.1313 found: 236.1311 [M^+].

EA(H_2)-TB

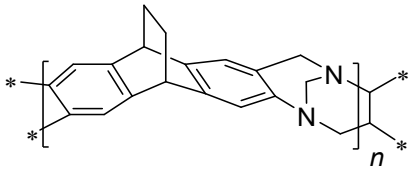

Under a nitrogen atmosphere, 9,10-dihydro-2,6(7)-diamino-9,10-ethanoanthracene (3.00 g, 13 mmol) was dissolved in dimethoxymethane (4.83 g, 63 mmol) and the solution cooled in an ice bath. Trifluoroacetic acid (25 ml) was added drop-wise over 30 min and the mixture was stirred for 24 h at room temperature. The viscous orange mixture was slowly poured into

aqueous ammonium hydroxide solution and stirred vigorously for 2 h during which a white solid was formed. The solid was collected by filtration, washed with water and then acetone until the washings were clear. The resulting white powder was dissolved in chloroform (50 ml) and methanol was added drop-wise until the solution became turbid. The solution was stirred for a further 30 min to precipitate a gel. The re-precipitation from chloroform was repeated twice. The crude polymer was dissolved in chloroform (50 ml) and added drop-wise to *n*-hexane (400 ml) with vigorous stirring and the precipitated fine powder was filtered. The white powder was refluxed in methanol for 24 h, filtered and then dried in a vacuum oven for 9 h to afford desired polymer (3.15 g, 91%) as a white powder. ^{1}H NMR (500 MHz, $CDCl_3$) δ 6.84 (br, m, 4H), 4.60 (br, s, 2H), 4.05 (br, s, 4H), 1.56 (s, br, 6H). ^{13}C NMR (100 MHz, solid state) δ_C 146.5 (br), 143.3 (br), 140.2 (br), 125.1 (br), 120.6 (br), 68.1 (br), 59.7 (br), 44.9 (br), 27.5 (br); GPC (Chloroform): Mn = 9,300, Mw = 49,500. BET surface area = 845 m^2/g; total pore volume = 0.62 cm^3/g at (P/P_0 = 0.9814); TGA analysis: Initial weight loss due to thermal degradation commences at ~ 260 °C with a 10% loss of mass below 400 °C consistent with the loss of an ethylene fragment from the ethanoanthracene unit via a retro Diels-Alder reaction and a further 24% mass loss below 1000 °C.

S3. Viscosity measurements

Intrinsic viscosities of PIM-EA(Me_2)-TB, PIM-EA(H_2)-TB, PIM-EA(Me_2)-TB/PAF-1, and PIM-EA(H_2)-TB/PAF-1 were measured using a Ubbelohde viscometer at 25 °C, and calculated based on the ATSM D445 standard. The pure 2 wt. % polymer solution contained 0.4 g polymer in 14 mL (20 g) of chloroform. Solutions containing PIM-EA(Me_2)-TB/PAF-1, and PIM-EA(H_2)-TB/PAF-1 were made up of 0.4 g PIM, and 0.04 g of PAF-1 in 20 g of chloroform.

S4. Gel permeation chromatography

Gel Permeation Chromatography was carried out using a Viscotek GPC Max1000 system which includes a refractive index detector and two 2 columns (KF-805L Shodex). The analysis used dilute solution of polymer in chloroform (1 ml min^{-1}).

Polymer	BET Surface area (m^2g^{-1})	Total Pore Volume [a] at (P/P_0) = 0.9814 (cm^3/g)	CO_2 Uptake [b] (cm^3/g)	Mw × 10^3 (g mol^{-1})	PDI
PIM-EA(H_2)-TB	845	0.62	77.2	49	5.3

Table S1. Summary of the physical properties of PIM-EA(H_2)-TB

[a] isothermal at 77 K. [b] isothermal at 273.15 K

S5. Scanning electron microscopy

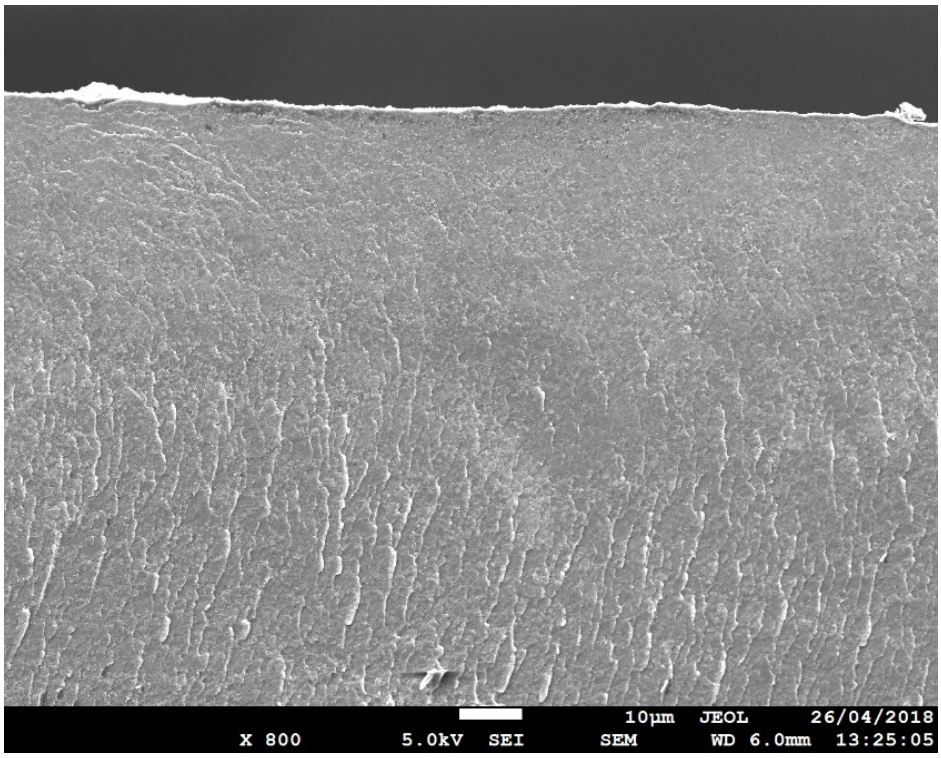

Figure S1. Low magnification (800x) of the cross section of a PIM-EA(H_2)-TB/PAF-1 film fractured in liquid nitrogen.

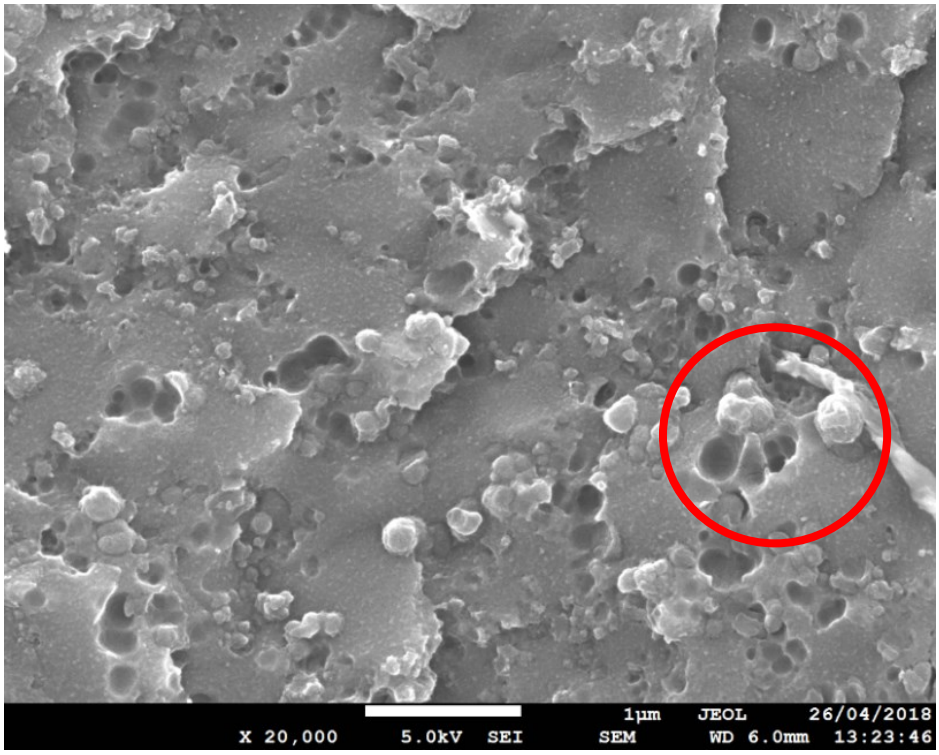

Agglomeration of PAF-1 nanoparticles

Figure S2. High magnification (20,000x) of the cross section of a PIM-EA(H_2)-TB/PAF-1 film fractured in liquid nitrogen. Larger cavities can be ascribed to the dislodged PAF-1 nanoparticles that agglomerated in the polymer matrix during cryo-facturing.

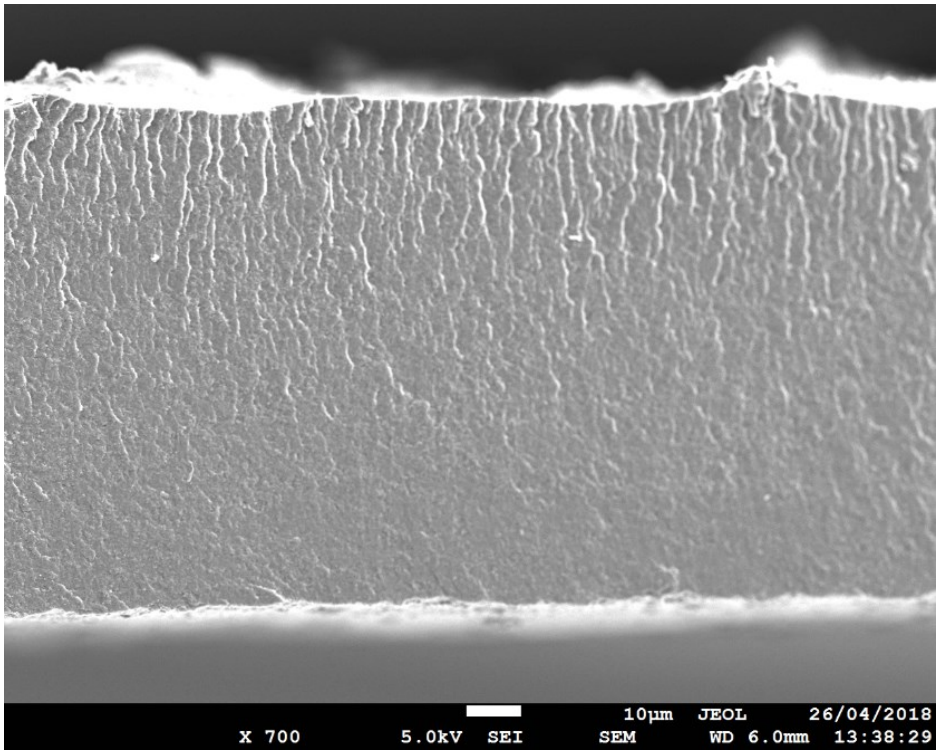

Figure S3. Low magnification (700x) of the cross section of a PIM-EA(Me_2)-TB/PAF-1 film fractured in liquid nitrogen.

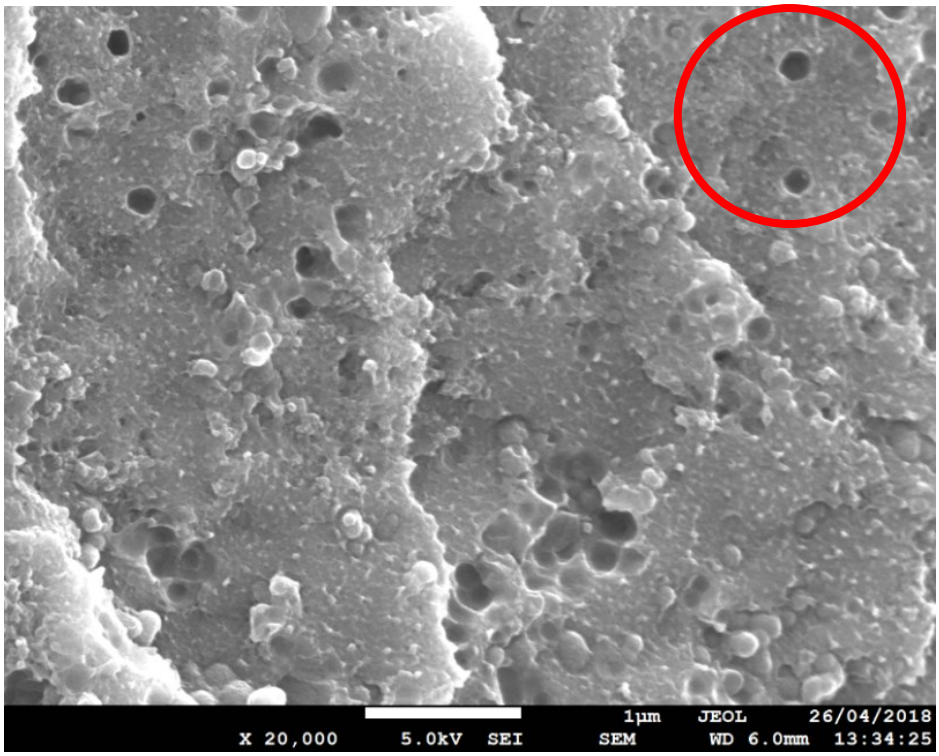

Better dispersion of PAF-1 nanoparticles

Figure S4. High magnification (20,000x) of the cross section of a PIM-EA(Me_2)-TB/PAF-1 film fractured in liquid nitrogen. Cavities (average diameter 200 nm) can be ascribed to the dislodged PAF-1 nanopartices during cryo-facturing. PAF-1 nanoparticles are dispersed better in PIM-EA(Me_2)-TB.

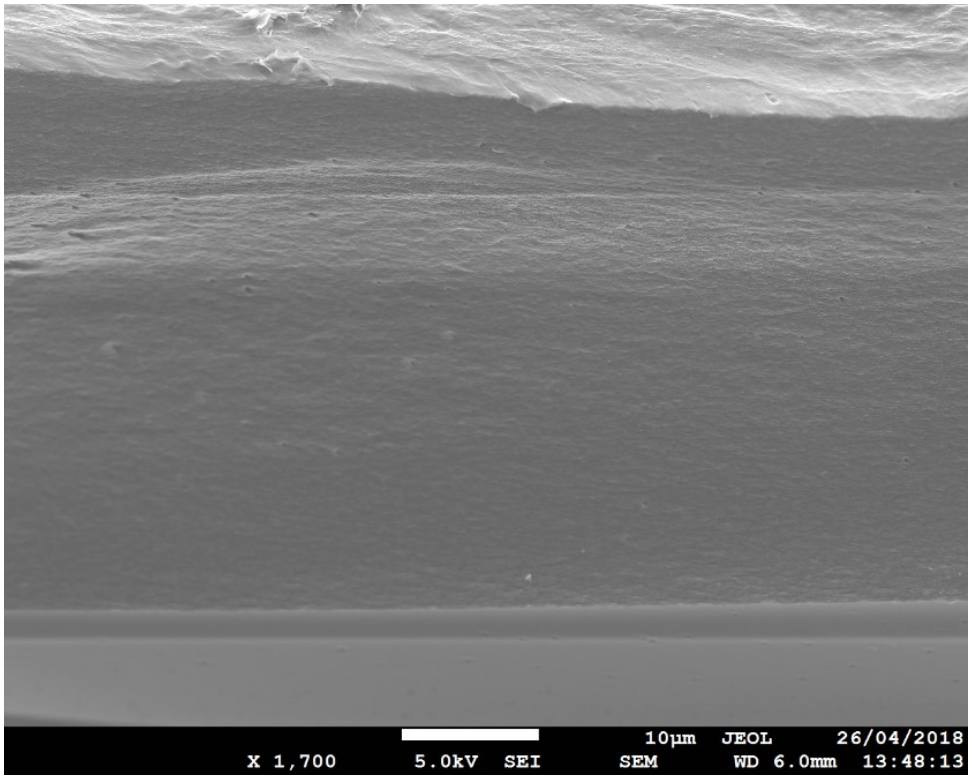

Figure S5. Low magnification (1,700x) of the cross section of a PIM-EA(H_2)-TB film fractured in liquid nitrogen.

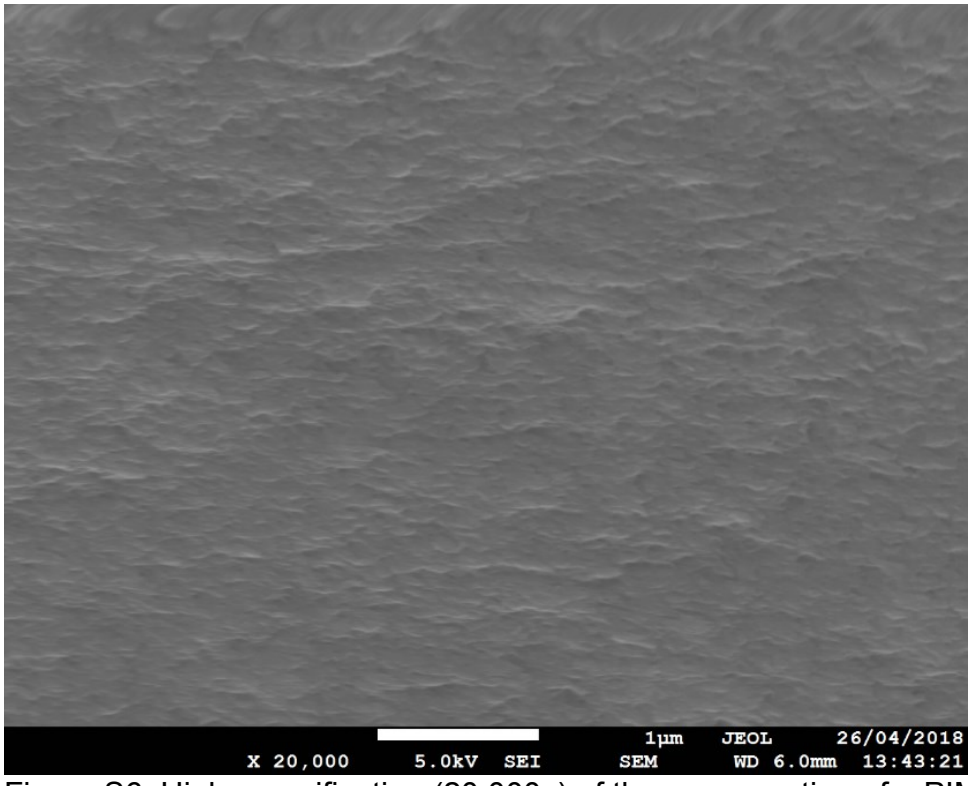

Figure S6. High magnification (20,000x) of the cross section of a PIM-EA(H_2)-TB film fractured in liquid nitrogen.

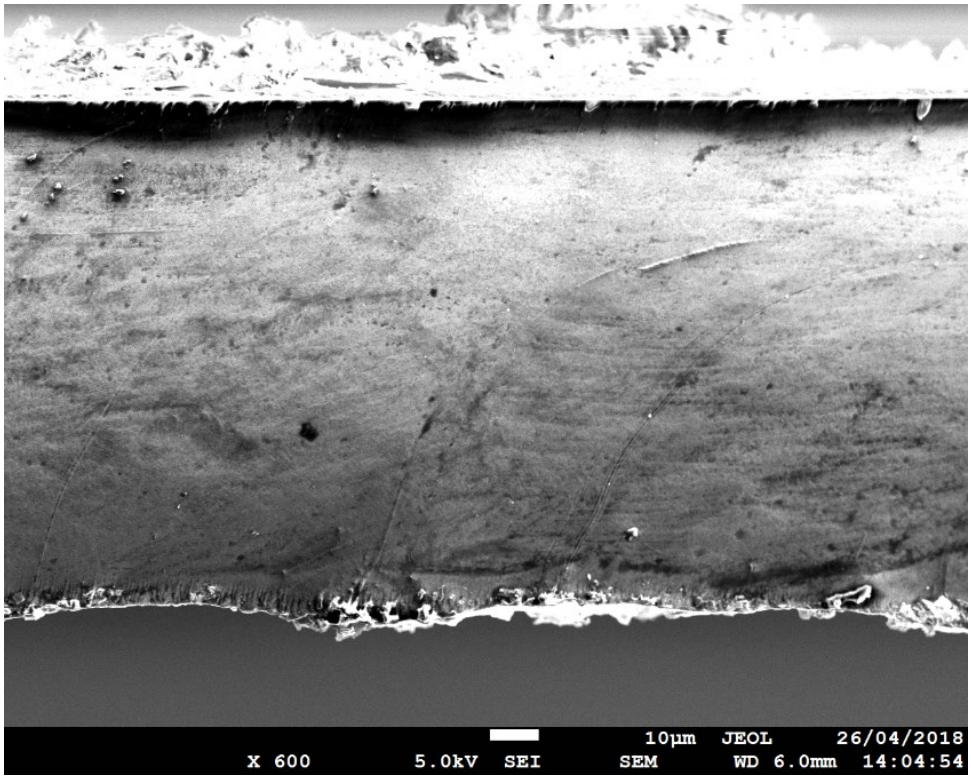

Figure S7. Low magnification (600x) of the cross section of a PIM-EA(Me_2)-TB film fractured in liquid nitrogen.

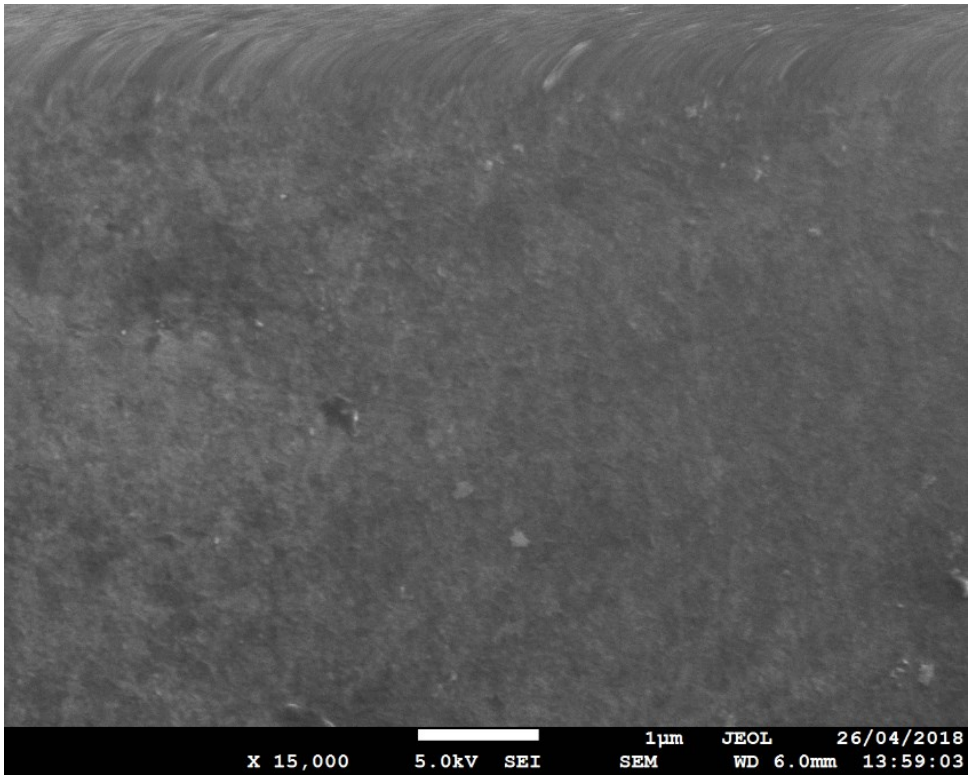

Figure S8. High magnification (15,000x) of the cross section of a PIM-EA(Me_2)-TB film fractured in liquid nitrogen.

S6. Gas adsorption

Low-temperature (77 K) N_2 adsorption/desorption measurements of PIM powders were made using a Coulter SA3100. Samples were degassed for 800 min at 120 °C under high vacuum prior to analysis at The University of Edinburgh. CO_2 adsorption at 273 K was measured using a volumetric system (QuantaChrome autosorb iQ2). The samples were degassed for 3 hours at 393 K prior the test. The data were analysed with the software provided with the instrument. NLDFT analysis was performed to calculate the pore size distribution and volume, considering a carbon equilibrium transition kernel at 273 K based on a slit-pore model; the kernel is based on a common, one centre, Lennard-Jones model.

The Brunauer-Emmett-Teller (BET) surface area of PAF-1 was determined using N_2 adsorption isotherms between 0 – 780 mmHg obtained from a Micrometrics ASAP 2420 instrument at CSIRO, Australia. PAF-1 samples were transferred to pre-dried analysis tubes, sealed with Transeal stoppers, evacuated and activated at 120 °C under a 10^{-6} dynamic vacuum for 24 hours. Ultra-high purity N_2 gas was used for these experiments. N_2 adsorption measurements were conducted at 77 K.

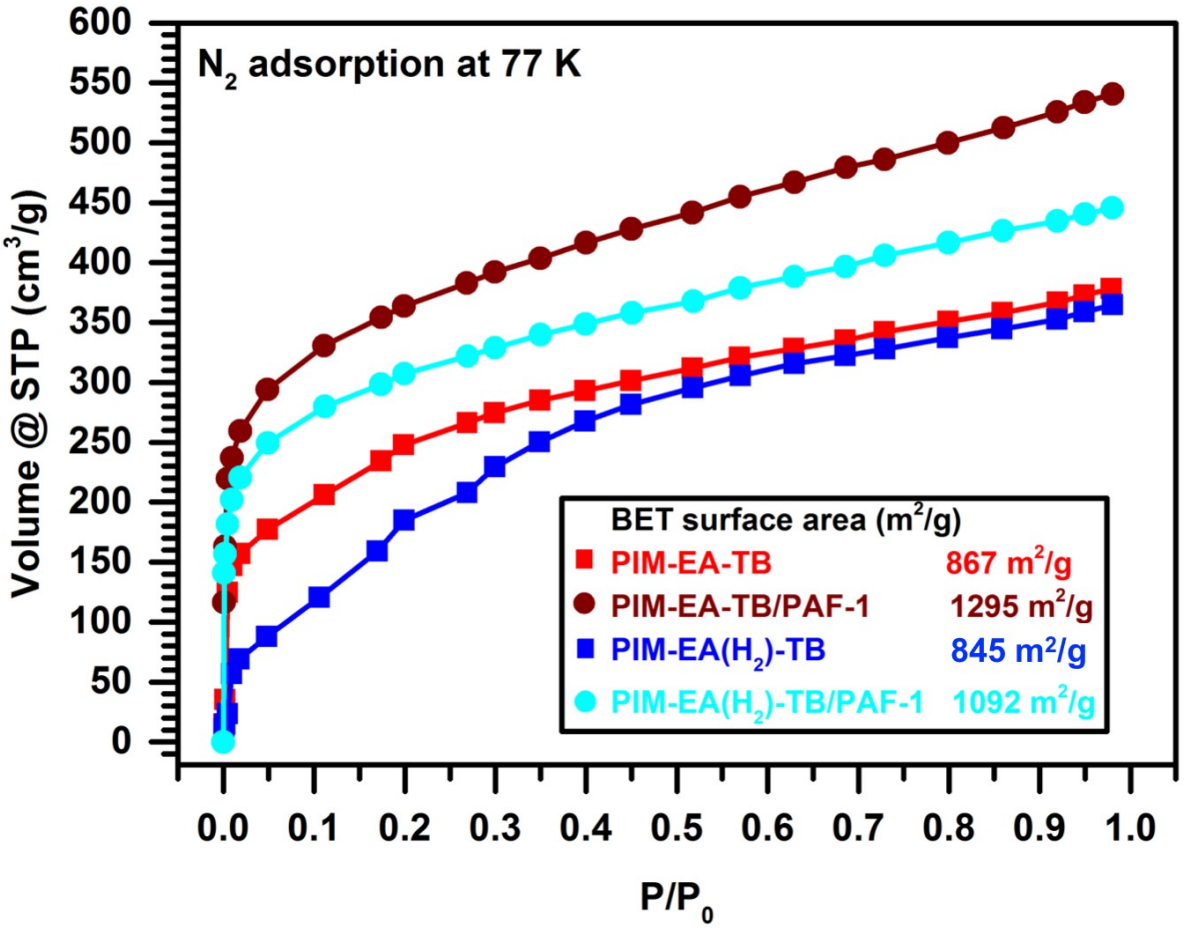

Figure S9. Nitrogen adsorption of PIMs and PIM/PAF-1 polymer blends studied here at 77 K.

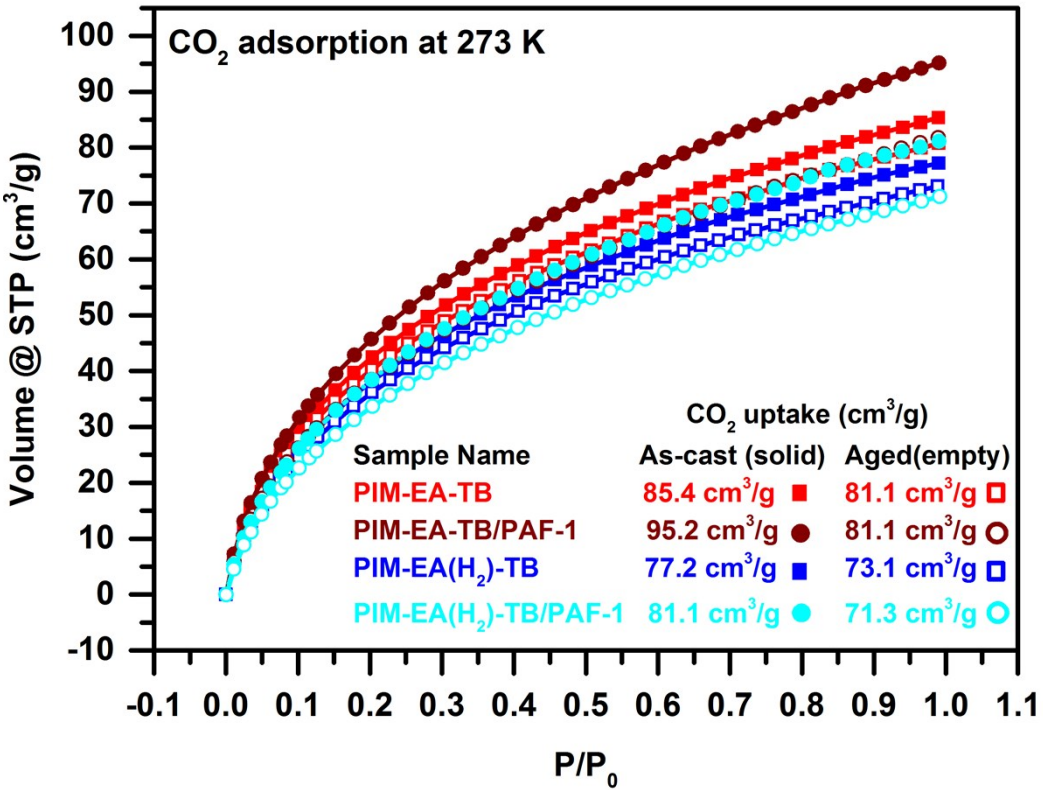

Figure S10. CO_2 adsorption of PIMs and PIM/PAF-1 polymer blends studied here at 273.15 K.

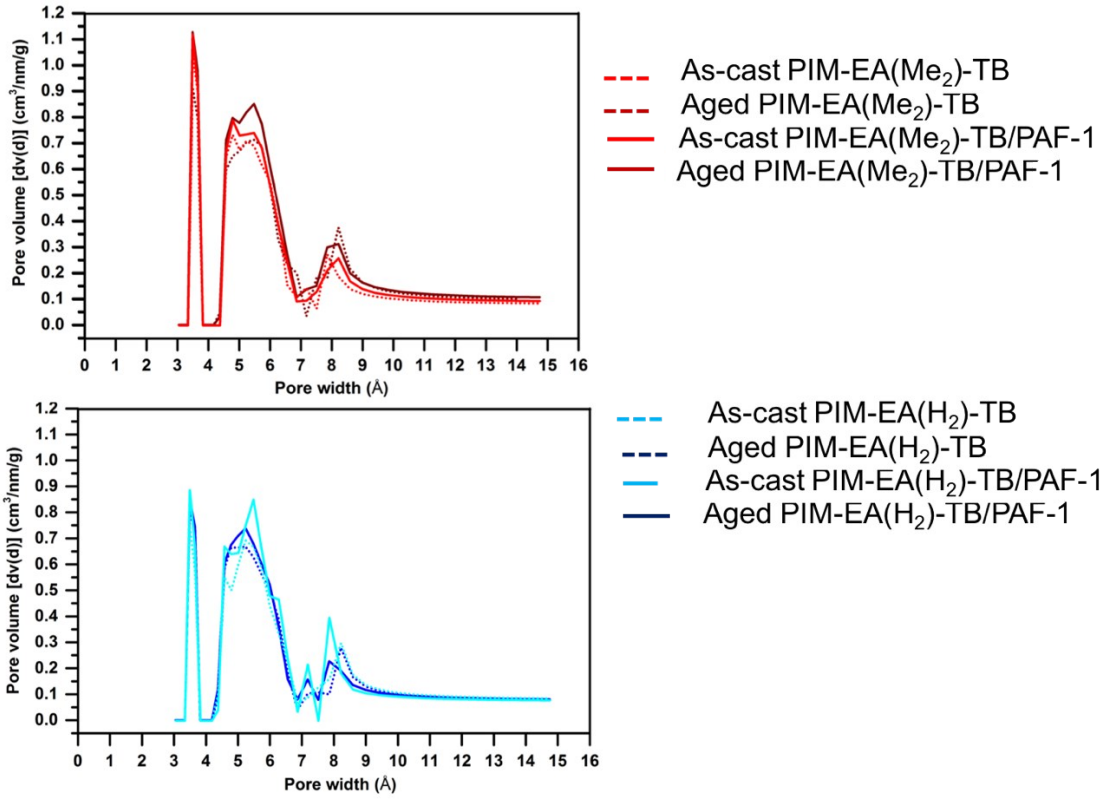

Figure S11. Pore size distribution of PIMs and their blends with PAF-1 studied here.

S7. Molecular Simulations using 3D-Chem

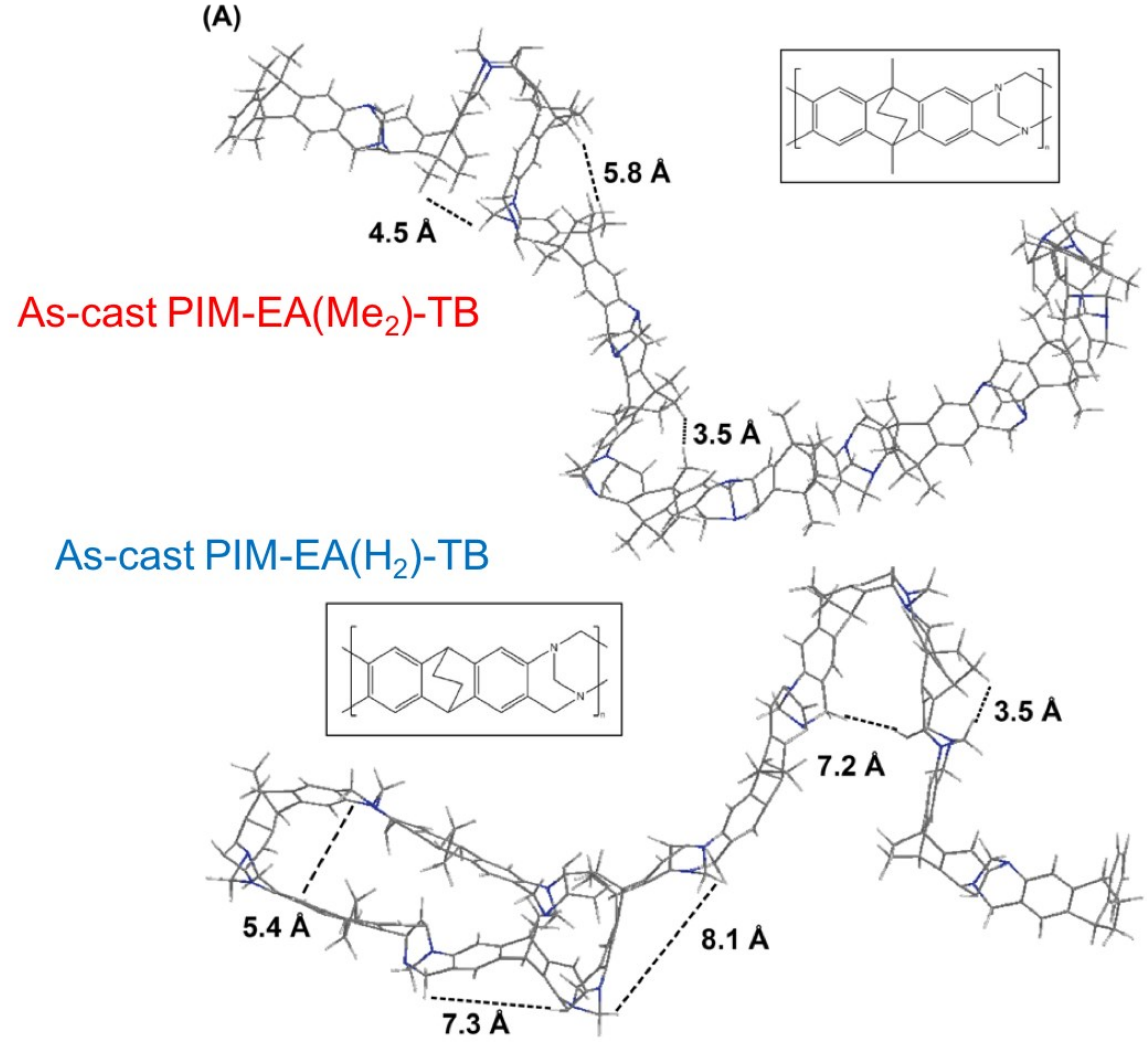

Figure S12. Molecular simulations of pore sizes in PIMs studied here.

S8. Positron Annihilation Lifetime Spectroscopy (PALS)

Bulk PALS experiments that were used to characterize changes in pore sizes in the material bulk were performed at CSIRO using an EG&G Ortec fast-fast coincidence system with fast plastic scintillators and a resolution function of 260 ps FWHM (^{60}Co source with the energy windows set to ^{22} Na events). Due to the long lifetimes, and the low counting rate, the coincidence unit was removed and the range of the TAC extended to 200 ns. The film samples were stacked to a thickness of 2 mm, and powdered samples were packed (>1.5 mm depth), on either side of a 30 μCi ^{22}NaCl source sealed in a 2.54 μm thick Mylar envelope (source correction 1.544 ns and 2.923%) and measured under vacuum at ~ 5 ∅ 10 $^{-7}$ Torr. At least five spectra of 4.5 million integrated counts were collected with each spectrum taking about 4.6 h to collect. Data analysis was performed using LT9. The spectra were best fitted with four components with the shortest lifetime fixed to 125 ps, characteristic of *p*-Ps annihilation. The Tao-Eldrup model[2,3] was used to calculate the mean pore sizes from mean *o*-Ps lifetimes.[4]

Sample	Aging (days)	τ_3 (ns)	τ_4 (ns)	I_3 (%)	I_4 (%)	Diameter 3 (nm)	Diameter 4 (nm)
PIM-EA(Me_2)-TB	0	1.99 ± 0.155	6.407 ± 0.069	5.12 ± 0.33	25.12 ± 0.46	0.569 ± 0.028	1.070 ± 0.005
	90	1.679 ± 0.164	6.407 ± 0.069	5.05 ± 0.18	24.68 ± 0.35	0.508 ± 0.035	1.040 ± 0.004
PIM-EA(Me_2)-TB/PAF-1	0	3.464 ± 0.200	8.359 ± 0.193	11.15 ± 0.99	21.67 ± 1.08	0.786 ± 0.024	1.209 ± 0.013
	90	3.561 ± 0.143	8.481 ± 0.223	13.27 ± 0.85	17.94 ± 0.97	0.798 ± 0.017	1.217 ± 0.014
PIM-EA(H_2)-TB	0	2.035 ± 0.179	6.176 ± 0.061	5.95 ± 0.30	28.29 ± 0.50	0.577 ± 0.032	1.051 ± 0.005
	90	1.701 ± 0.098	5.691 ± 0.029	5.34 ± 0.23	26.83 ± 0.24	0.512 ± 0.020	1.011 ± 0.002
PIM-	0	3.582 ± 0.240	8.428 ± 0.301	13.11 ± 1.43	20.16 ± 1.52	0.800 ± 0.029	1.214 ± 0.020

90	3.693 ± 0.064	8.695 ± 0.146	15.54 ± 0.50	15.97 ± 0.48	0.813 ± 0.007	1.231 ± 0.009

Table S2 Lifetimes and intensities of pore size distributions of PIMs and PIM/PAF-1 systems studied here were obtained from bulk positron annihilation lifetime spectroscopy (PALS).

Sample	Aging (days)	FFV content (%)	ΔFFV due to aging (%)	ΔFFV due to methyl replacement (%)
PIM-EA(Me_2)-TB	0	29.9	- 14	-
	90	26.8		
PIM-EA(Me_2)-TB/PAF-1	0	41.2	- 10	-
	90	36.9		
PIM- EA(H_2)-TB	0	32.1	-16	7
	90	26.8		
PIM- EA(H_2)-TB/PAF-1	0	40.3	- 11	-
	90	36		

Table S3 FFV content of PIM and PIM/PAF-1 blends studied here is obtained from bulk positron annihilation lifetime spectroscopy (PALS).

S9. Small angle/Wide angle x-ray spectroscopy (SAXS/WAXS)

Raw data obtained from the Australian Synchrotron is represented by circles, and the dashed orange line is a fit of the sum of all Gaussian curves ascribing to various pore size distributions. Inter-chain distance is represented by the dark blue line, while the intra-chain pores are represented by both green and purple lines. Pores ascribed to distances between ethylene and methylene bridges are assigned by orange and light blue lines.

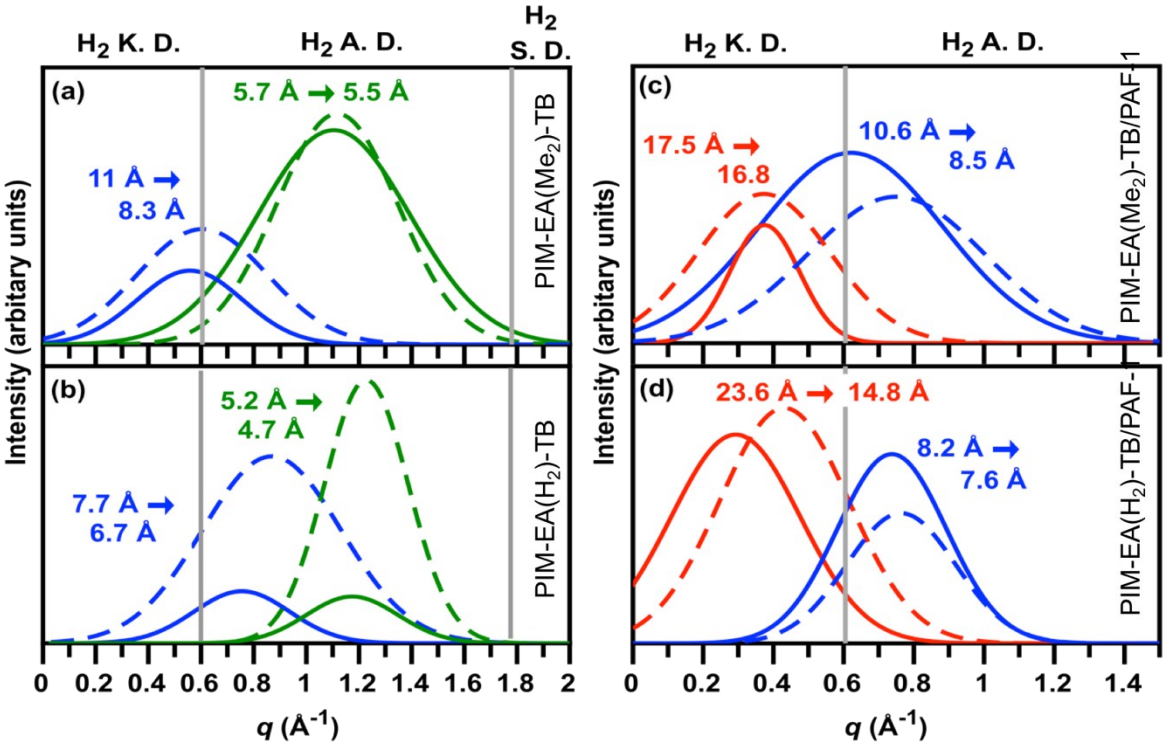

Figure S13 SAXS/WAXS spectra were obtained at the Australian Synchrotron, and full analyses of these spectra are found in the Supporting Information (Fig. S7 – S10). Raw data was fitted with a sum of Gaussian plots using MagicPlot to obtain various pore size distributions (as-cast samples – solid lines, aged samples – dashed lines). (a) Methyl groups in PIM- EA(Me_2)-TB enlarge inter-PIM chain distances *i.e.* *d*-space (blue) that are reduced by 24 % during aging. (b) Smaller hydro groups reduce *d*-space in PIM- EA(H_2)-TB that is less prone to physical aging. Intra-chain distances (green) in PIM- EA(H_2)-TB are more prone to physical aging as well. (c) PAF-1 creates an additional pore size distribution (red) but abates *d*-space shrinkage in PIM- EA(Me_2)-TB over time. (d) The additional pore size distribution (red) is significantly larger in PIM- EA(H_2)-TB/PAF-1, and more prone to physical aging.

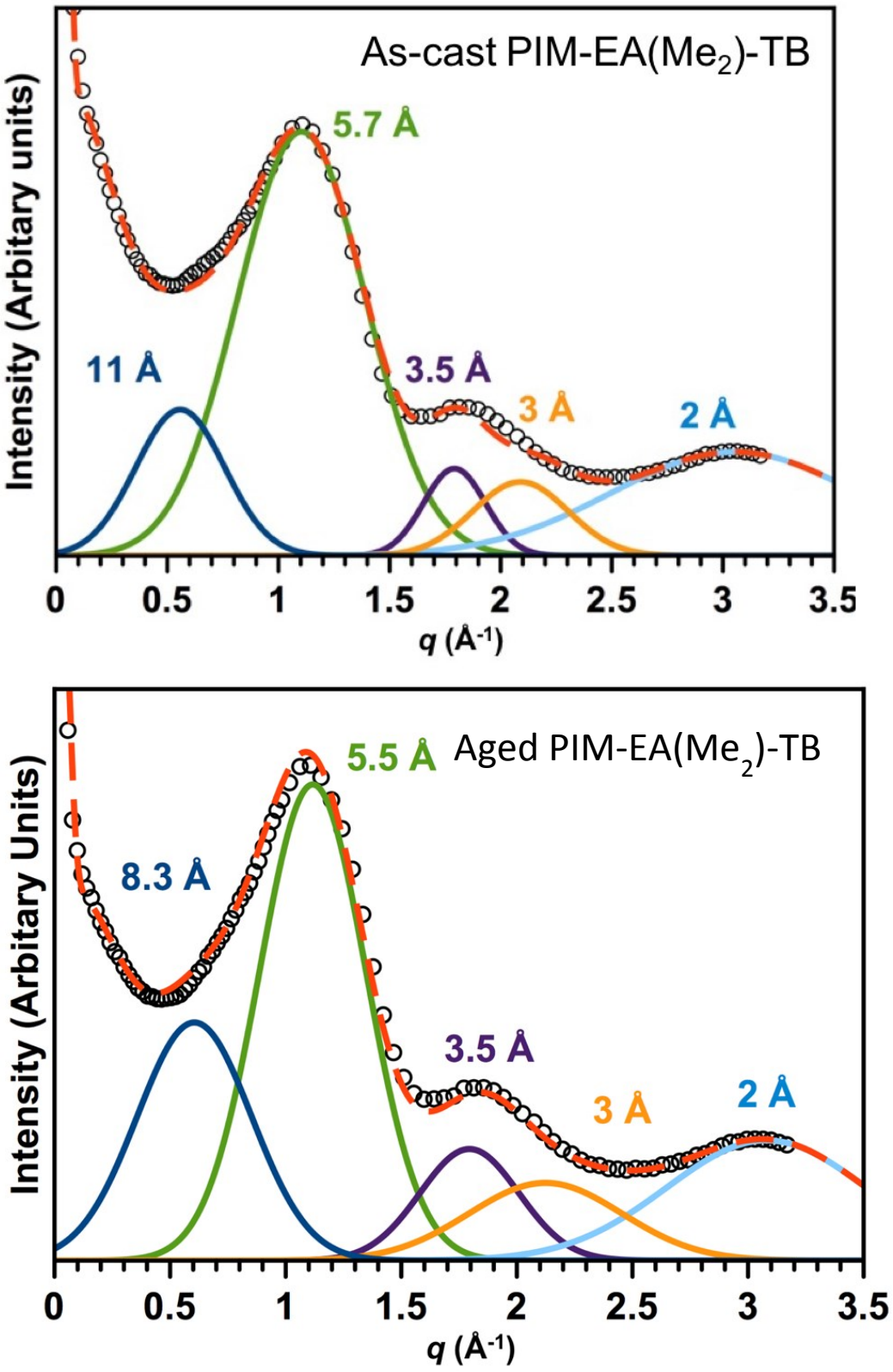

Figure S14. SAXS/WAXS spectra of as-cast and aged (90 days) of PIM- EA(Me_2)-TB films.

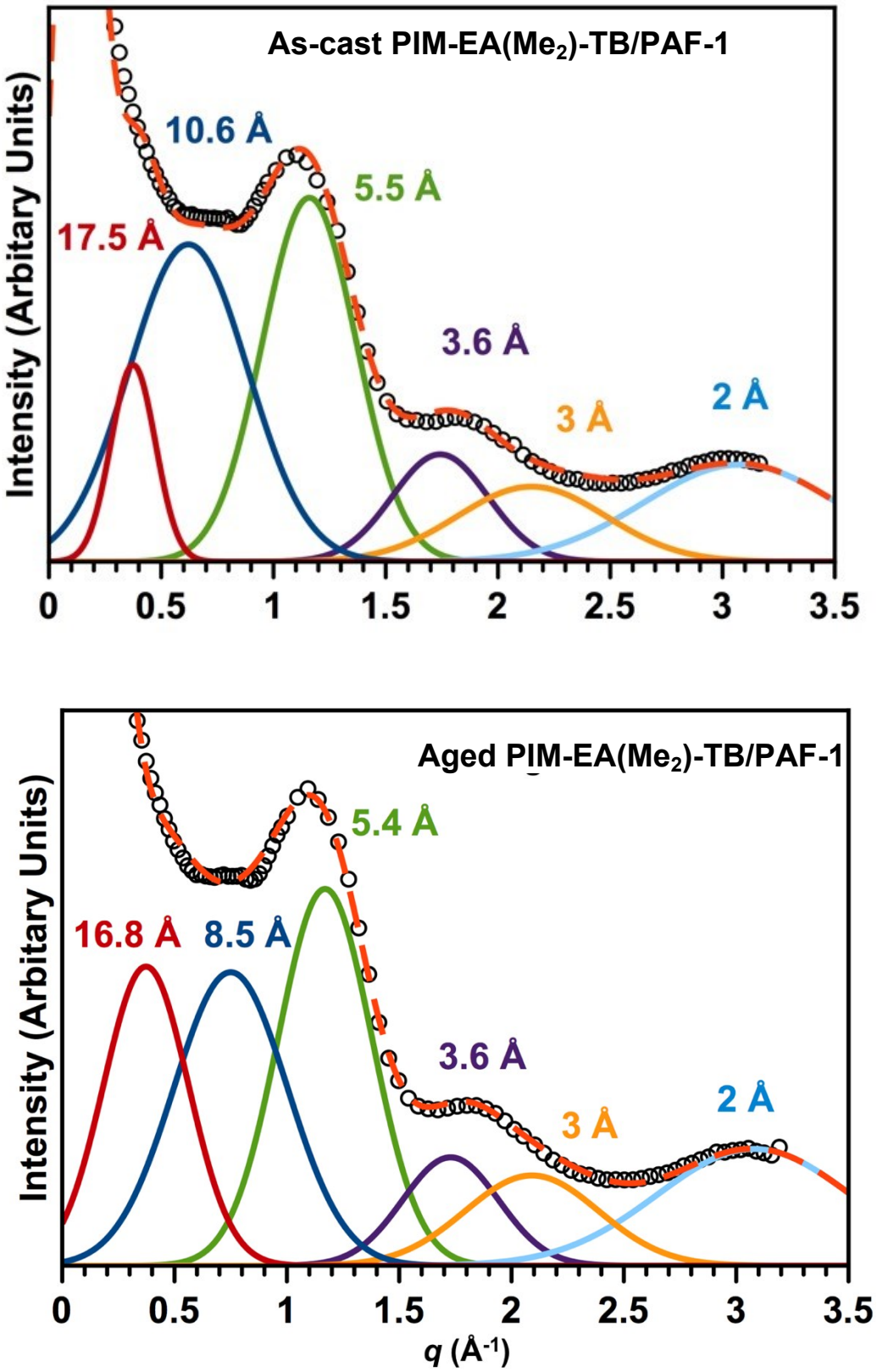

Figure S15. SAXS/WAXS spectra of as-cast and aged (90 days) of PIM- EA(Me_2)-TB/PAF-1 films.

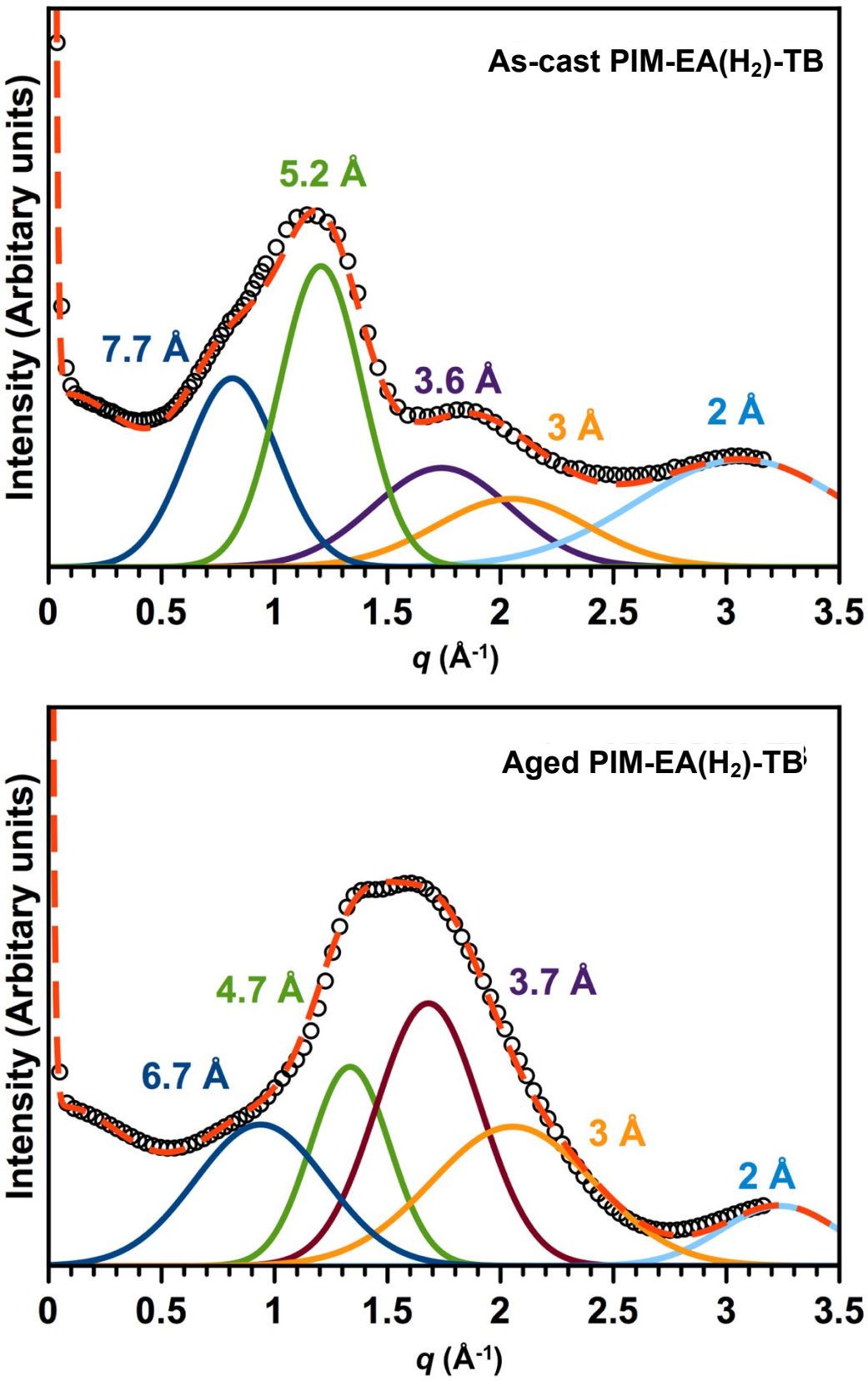

Figure S16. SAXS/WAXS spectra of as-cast and aged (90 days) of PIM- EA(H_2)-TB films.

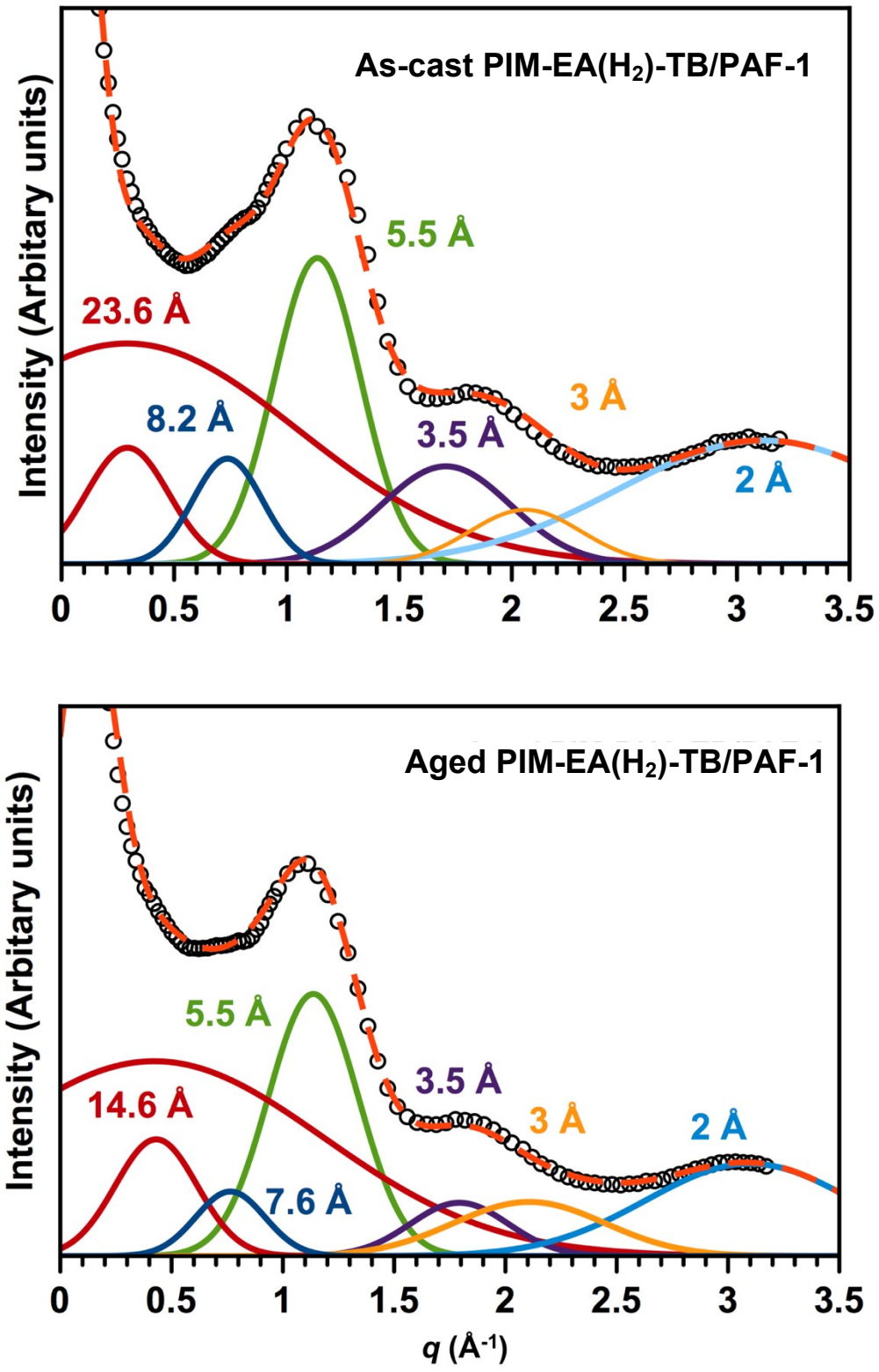

Figure S17. SAXS/WAXS spectra of as-cast and aged (90 days) of PIM- EA(H_2)-TB/PAF-1 films.

S10. ^{13}C solid state nuclear magnetic resonance spectroscopy

The causes of pore size and concentration reduction (lower FFV content) due to aging in both PIMs and their nanocomposites were investigated using solid state ^{13}C NMR. The loss in pore concentration and pore size reduction is indirectly linked to polymer chain mobility.[5] As polymer chains became mobile during physical aging, the FFV content between these chains are reduced. The T_1 relaxation times of various CH_x units (CH_3 groups on EA units in PIM- EA(Me_2)-TB, methylene bridges (CH_2) in both PIMs, and CH moieties on benzene rings) in PIMs studied here were correlated to their mobilities. Relative decreases in T_1 values corresponded to enhanced atom mobility, while relative increases in T_1 values signified lower atom mobility.[5] The T_1 relaxation times of carbon atoms in as-cast polymer films were set as 0 %. Carbon atoms of the dimethyl groups (C9) and methylene bridge (C7) on the EA unit, and the methylene bridge (C1) of the TB unit became more mobile during physical aging; particularly C9 as its T_1 was reduced by 60 %. This was also observed in other PIMs and super glassy polymers during physical aging.[6,7] The mobility of these bulky carbon atoms were as follows: C9 > C7 > C1. The reduction of free-space between polymer chains during physical aging restricted main chain carbon atom movements (C3 – 6 T_1 relaxation times increased). PAF-1 reduced C9 mobility, while completely immobilizing C1 and C7 atoms in as-cast PIM- EA(Me_2)-TB/PAF-1 films. This pin-pointed the interaction locations between PAF-1 and PIM- EA(Me_2)-TB chains – the methylene bridges.

Physical aging enhanced the mobility of main chain carbons C3, C4, and C6, and C7 of the methylene bridge on the EA(H_2) unit in PIM- EA(H_2)-TB. Without bulky methyl groups on the EA unit to prop apart PIM- EA(H_2)-TB chains, PAF-1 were unable to infiltrate between PIM- EA(H_2)-TB polymer chains, and interact with the methylene group on the TB unit. Thus, PAF-1 only reduced the mobility of C7 – the carbon atom on the methylene bridge of the EA unit, leaving C1 – the methylene carbon atom on the TB unit untethered. The physically tethered EA(H_2) unit rigidified the TB unit that consequently reduced mobilities of the main chain atoms C3 – C6.

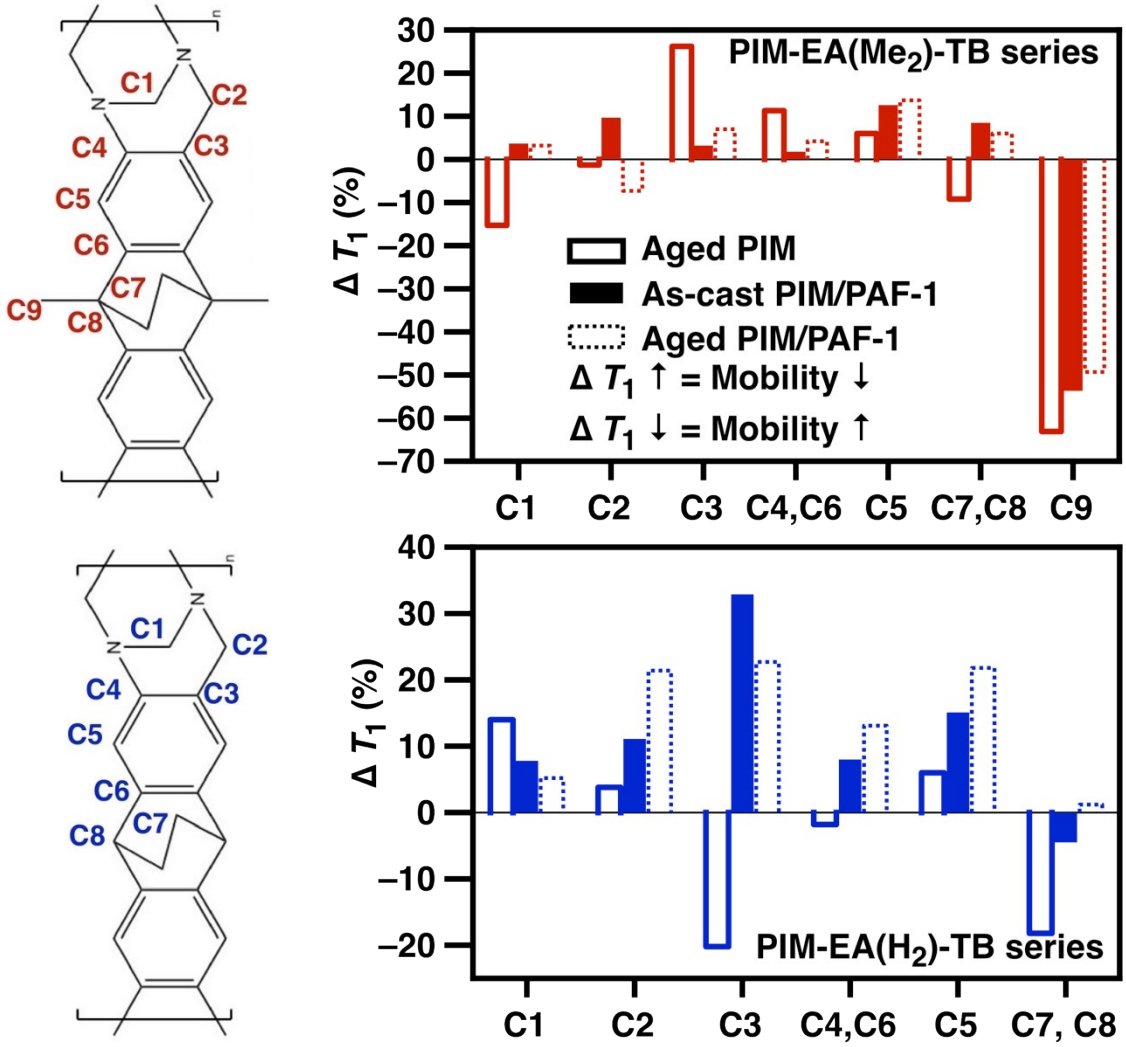

Figure S18 Solid state ^{13}C NMR T_1 relaxation times of (b) PIM- EA(Me_2)-TB and (c) PIM- EA(H_2)-TB. Relative changes to T_1 values are referenced to the T_1 relaxation times of as-cast PIMs which are set as 0 %. As-cast samples were characterized immediately after film formation *via* solution casting. Samples were aged for 90 days prior NMR characterization.

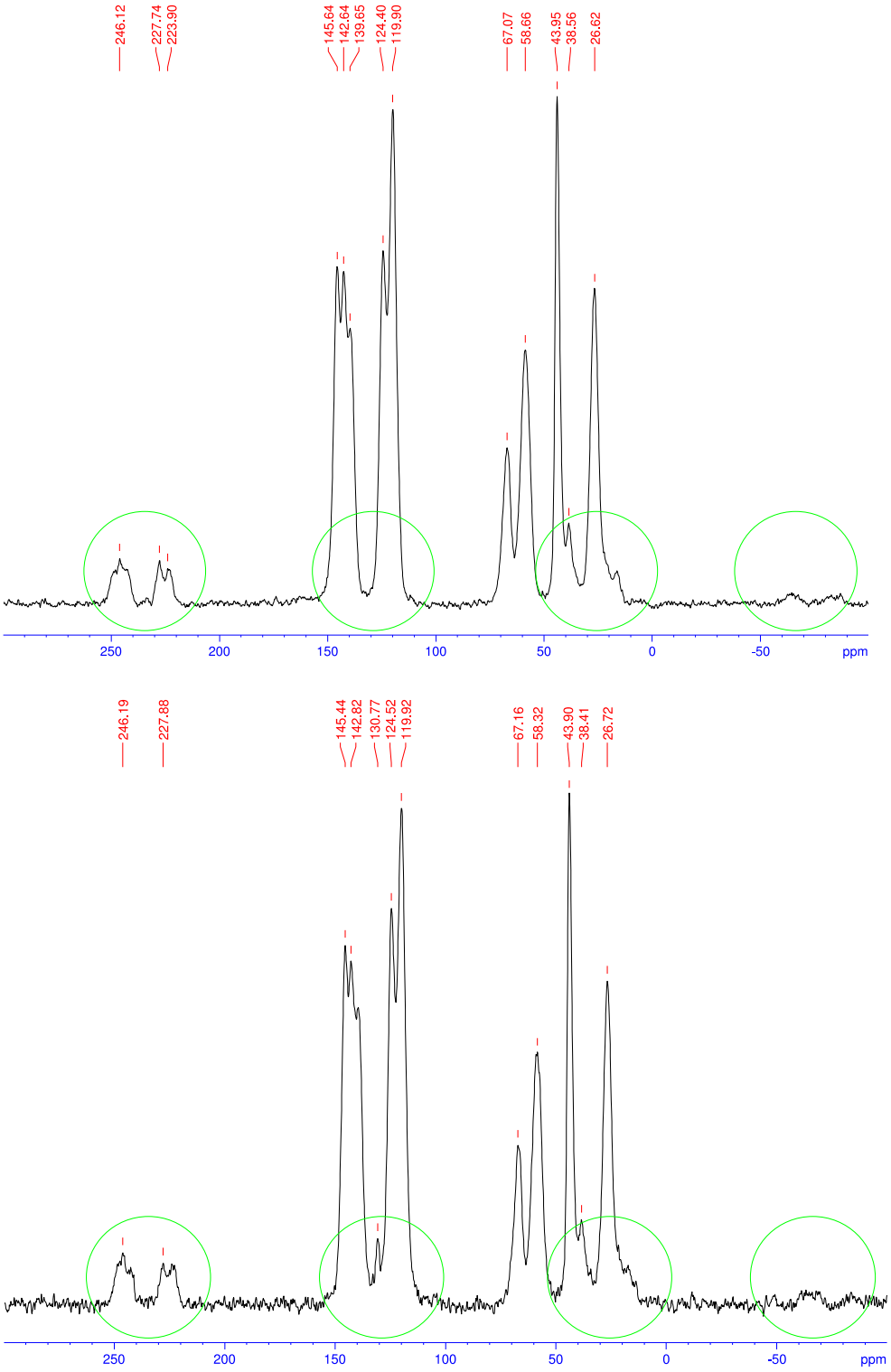

Figure S19 Solid state ^{13}C NMR *spectra* of as-cast (b) PIM- EA(H_2)-TB and (c) PIM-EA(H_2)-TB/PAF-1 blends. The blending of PAF-1 did not lead to any chemical shifts in peak positions – indicating an absence of chemical interactions between PAF-1 and the PIM matrix.

Table S4 T_1 relaxation times of carbon atoms in PIMs and PIM blends studied here.

	164-134 ppm		134 -97 ppm		90.5-64 ppm		64.6-50.8 ppm		50.8-33.7 ppm		33.7- 7.85 ppm	
Sample Name	T_1 values (s)	Change in T_1 (%)	T_1 values (s)	Change in T_1 (%)	T_1 values (s)	Change in T_1 (%)	T_1 values (s)	Change in T_1 (%)	T_1 values (s)	Change in T_1 (%)	T_1 values (s)	Change in T_1 (%)
As-cast PIM- EA(H_2)-TB	3.178		2.896		2.901		3.097		3.507		3.283	
Aged PIM- EA(H_2)-TB	3.369	6.0	2.845	-1.8	2.314	-20.2	3.216	3.8	3.999	14.0	2.685	-18.2
As-cast PIM- EA(H_2)-TB/PAF-1	3.659	15.1	3.127	8.0	3.856	32.9	3.44	11.1	3.782	7.8	3.135	-4.5
Aged PIM- EA(H_2)-TB/PAF-1	3.872	21.8	3.274	13.1	3.56	22.7	3.761	21.4	3.691	5.2	3.323	1.2
		5.8		4.7		-7.7		9.3		-2.4		6.0

	157-132 ppm		132-121 ppm		121-109 ppm		83-64 ppm		64-47 ppm		48-28 ppm		28-4.03 ppm	
Sample Name	T_1 values (s)	Change in T_1 (%)	T_1 values (s)	Change in T_1 (%)	T_1 values (s)	Change in T_1 (%)	T_1 values (s)	Change in T_1 (%)	T_1 values (s)	Change in T_1 (%)	T_1 values (s)	Change in T_1 (%)	T_1 values (s)	Change in T_1 (%)
As-cast PIM-EA(Me_2)-TB	2.796		2.504		2.303		2.976		3.014		2.577		0.337	
Aged PIM-EA(Me_2)-TB	2.963	6.0	2.786	11.3	2.906	26.2	2.938	-1.3	2.553	-15.3	2.340	-9.2	0.124	-63.1
As-cast PIM-EA(Me_2)-TB/PAF-1	3.148	12.6	2.548	1.8	2.377	3.2	3.265	9.7	3.125	3.7	2.796	8.5	0.156	-53.7
Aged PIM- EA(Me_2)-TB/PAF-1	3.18	13.7	2.61	4.2	2.465	7.0	2.758	-7.3	3.11	3.2	2.732	6.0	0.171	-49.3
		1.0		2.4		3.7		-15.5		-0.5		-2.3		9.7

S11. Gas permeabilities of PIMs and PIM/PAF-1 polymer blends

Single gas permeabilities at 2 atm were determined from the rate of downstream pressure build-up rate (*dp*/*dt*) obtained when permeation reached a steady state according to the following equation:

$$P = D \times S = \frac{273 \times 10^{10}}{760} \frac{VL}{AT[\frac{p_2 \times 76}{14.7}]} (\frac{dp}{dt})$$

P refers to the permeability of a membrane to a gas and its unit is in Barrer (1 Barrer = 1 × 10^{-10} cm^3 (STP)-cm/cm^2 sec cmHg), D is the average effective diffusivity (cm^2/s), S is the apparent sorption coefficient/solubility (cm^3 (STP)/cm^3 polymer cmHg), V is the volume of the downstream chamber (cm^3), L is the film thickness (cm). A refers to the effective area of the membrane (cm^2), T is the experimental temperature (K) and the pressure of the feed gas in the upstream chamber is given by p_2 (psia).

Physical aging of films studied here were tracked by periodic single-gas permeability measurements. All samples were stored in ambient conditions in a covered petri dish on lab benches between each permeability measurement test. This method of characterizing physical aging will demonstrate the true effect of polymer chain mobility over time, and not due to operating conditions (for e.g. constant exposure to gases).

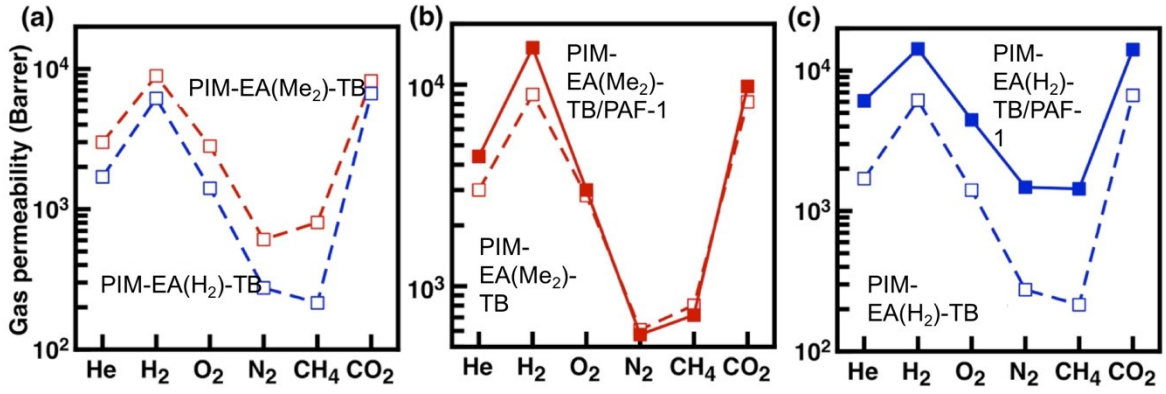

Figure S20 (a) Without methyl groups to prop PIM chains apart, the gas permeabilities of PIM-EA(H_2)-TB are lower, particularly for the larger gases such as N_2 and CH_4. (b) PAF-1 enhances He, H_2, O_2 and CO_2 permeabilities, while reducing N_2 and CH_4 gas permeabilties in PIM-EA(Me_2)-TB. c) All PIM- EA(H_2)-TB gas permeabilities are enhanced by PAF-1, particularly for N_2 and CH_4. Pure gas permeation data were obtained from two different laboratories (CSIRO, Hill group; and UoE, Ferrari group). The standard deviation between data from two groups is 5 %; highlighting the accuracy of real gas separation performances of these membranes. Membranes with an average thickness of 100 µm are used here for characterization at 2 bar. Each data point represents an average of three measurements. Lines are drawn to guide the eye, and permeability values are ± 5 % within standard deviation.

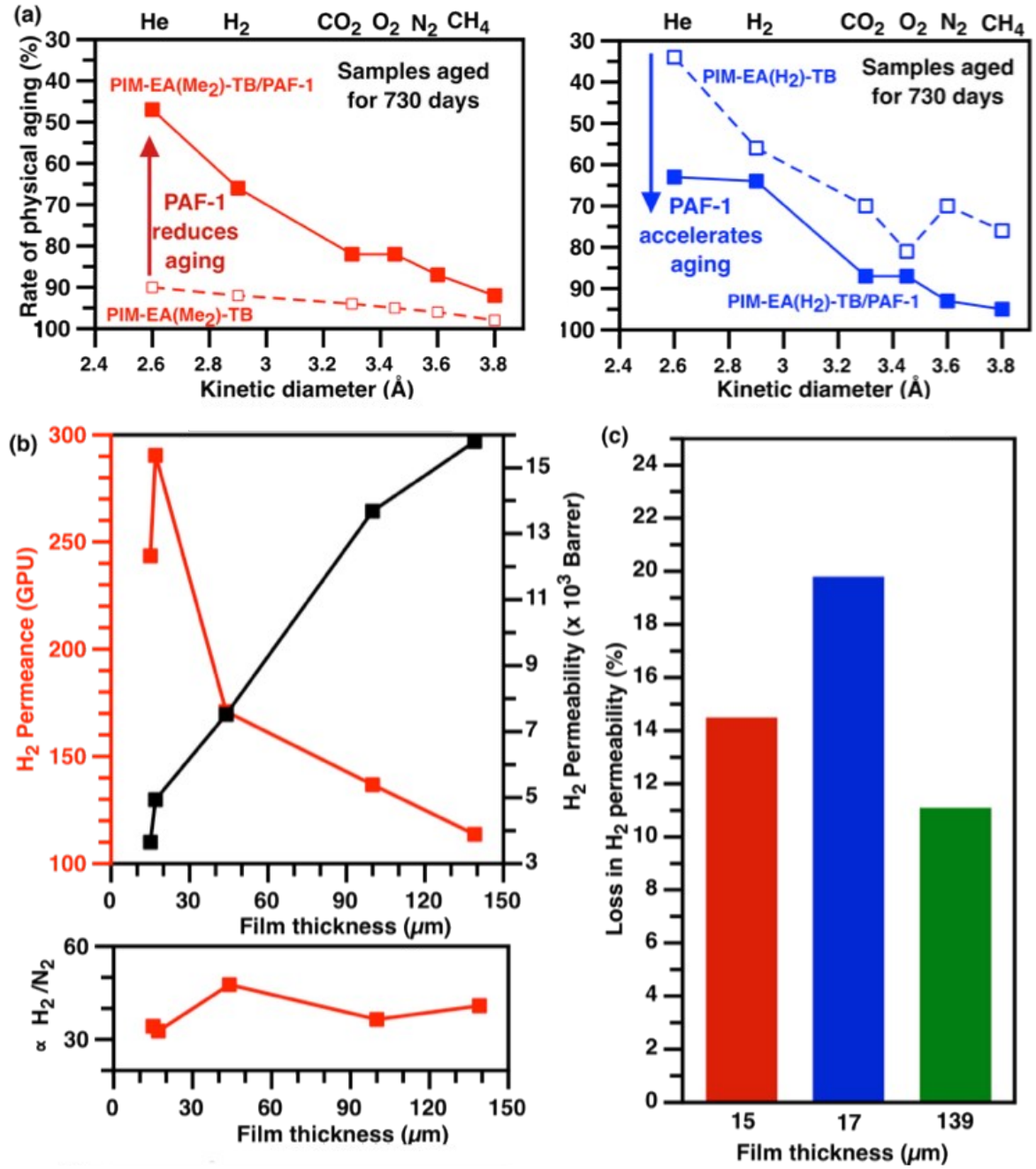

Figure S21 (a) The impact of physical aging on single gas permeability losses in PIM-EA(Me2)-TB (□), PIM-EA(Me2)-TB/PAF-1 (□), PIM-EA(H2)-TB (□), and PIM-EA(H2)-TB/PAF-1 (□) Physical aging over 730 days leads to drastic gas permeability losses (> 90 %) in both PIMs. The incorporation of PAF-1 into PIM-EA(Me2)-TB largely retains He and H2 permeabilities, but does not stop the losses in O2, N2, CO2, and CH4 permeabilities. Meanwhile PAF-1 accelerates physical aging in PIM-EA(H2)-TB, leading to more significant losses in all gas permeabilities. (b) The effect of film thickness on single gas H2 permeabilities of PIM-EA(Me2)-TB/PAF-1. (c) The losses in H2 permeability due to physical aging in PIM-EA(Me2)-TB/PAF-1 films with different thicknesses are consistent throughout thick and thin films.

Using a previously published protocol and equipment from the Freeman group,[8] as illustrated in the Figure below, CO_2/CH_4 mixed gas permeabilities were measured. Two mass flow controllers (MFCs) (Model F-231M, Bronkhorst USA, Bethlehem, PA, USA) were used to regulate the influx of the upstream gas mixture. Mixed-gas permeability coefficients were

determined at total feed pressure ranging from 4 to 40 atm for CO_2/CH_4 mixture containing 50 mol. % CO_2. All measurements were conducted at 35 ℃.

The upstream pressure in the system was measured using a 1,000 psig pressure transducer (Honeywell Sensotec, Columbus Ohio, USA). A custom-built permeation cell, which contains a flow distributor, was used to prevent the concentration polarization at the upstream face of the membrane. The downstream pressure was atmospheric (0 psig), and a carrier gas (Helium) was used to sweep the permeate gas molecules away from the membrane surface to gas chromatograph (GC). Using an Agilent 6890 GC (Agilent Technologies, Santa Clara, CA, USA) with a thermal conductivity detector (TCD), the gas composition in the permeate stream was determined. All data from these measurements were collected when the steady state transmembrane flux was reached, and the stage cut (i.e., the ratio of the feed flow rate to the permeation rate) was less than 0.1 %. Permeability was calculated using the following equation:

$$P_A = \frac{x_{1A} S}{x_{He}^{P} A \left(p_2 x_{2A} - p_1 x_{1A}\right)} l$$

Where P_A is the permeability coefficient of component A, S is the sweep gas (Helium) flow rate, x_{1A} and x_{2A} are the mole fractions of component A in the permeate stream and feed streams, respectively; x_{He}^{P} is the mole fraction of helium in the permeate stream, P_2 is the feed stream pressure, P_1 is the permeate stream pressure, A is the area of the membrane, and l is the membrane thickness.

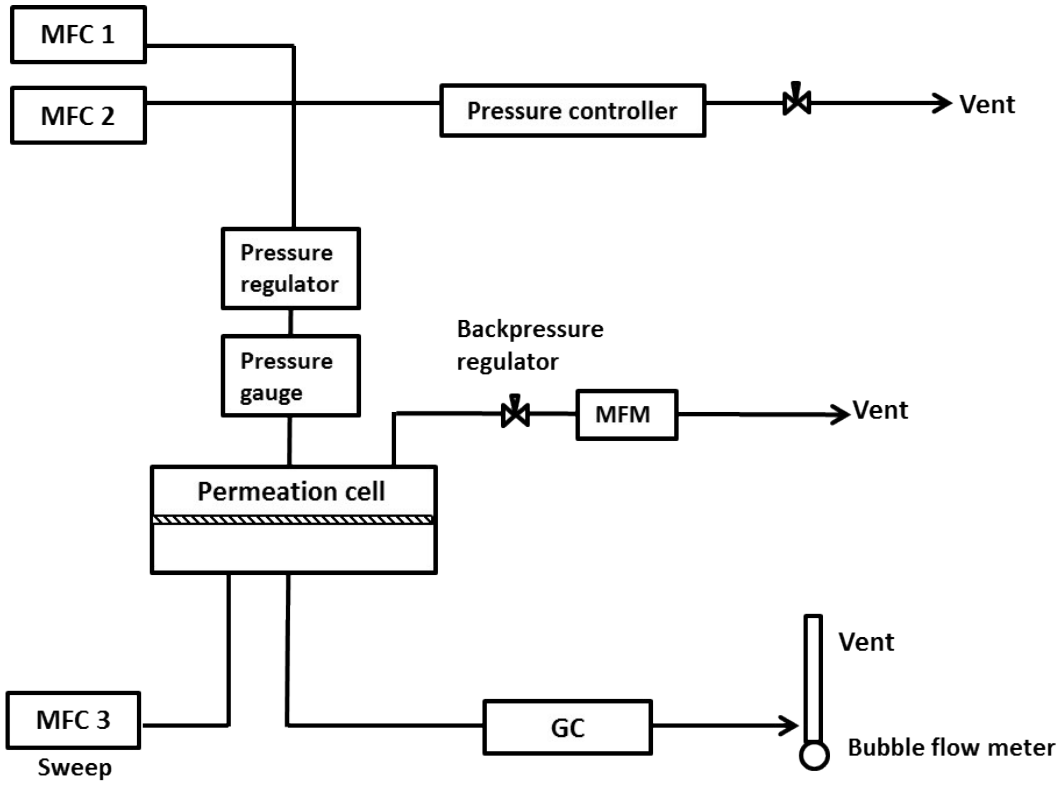

Figure S22 Schematic of mixed gas permeation setup at UT, Austin deployed in this work.

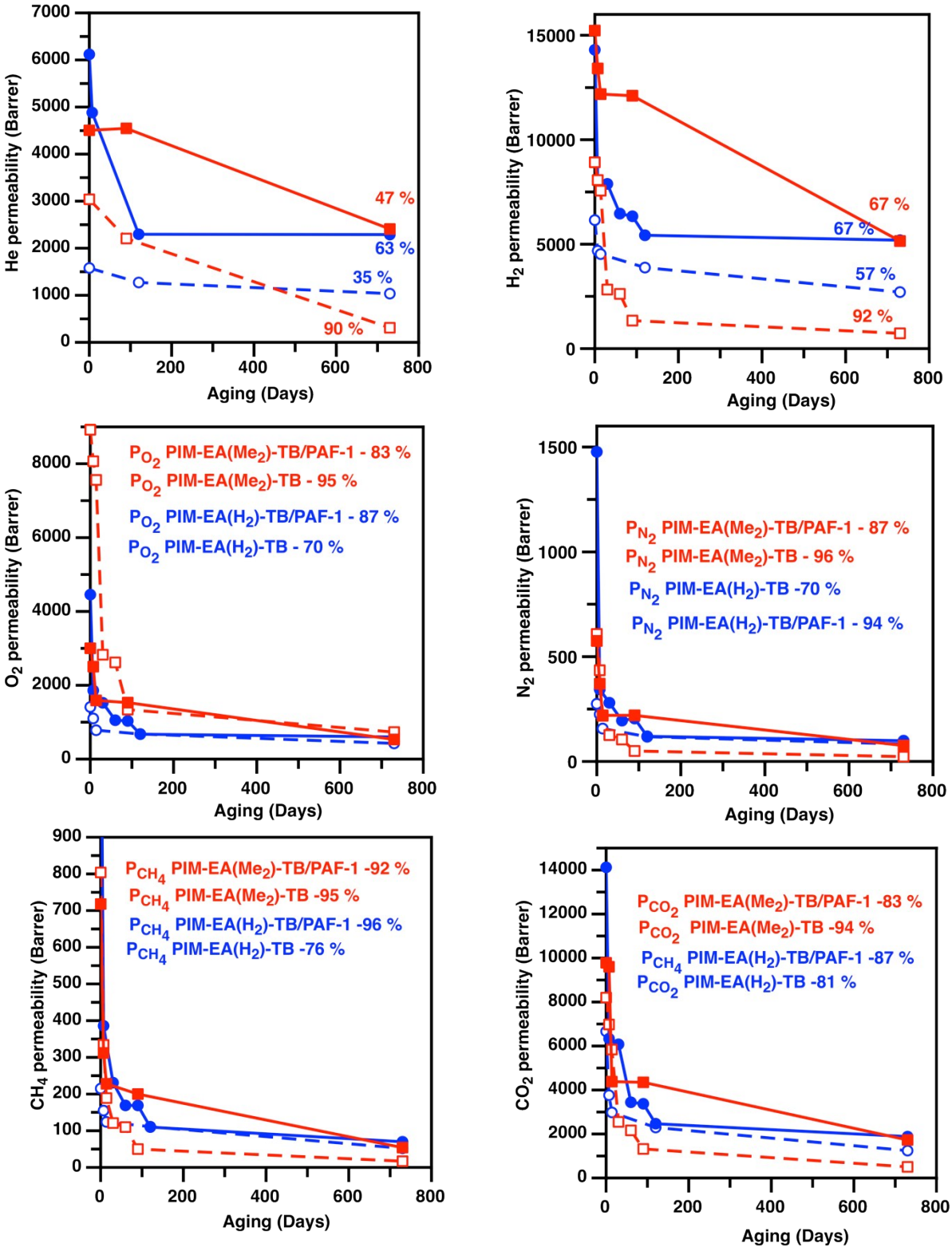

Figure S23. Pure gas permeabilities of PIM-EA(Me_2)-TB (○), PIM-EA(Me_2)-TB/PAF-1 (●), PIM- EA(H_2)-TB (□), and PIM-EA(H_2)-TB/PAF-1 (■) are reduced over 90 days of physical aging. The gas permeability values represent an average of 3 measurements with ± 5 % deviation.

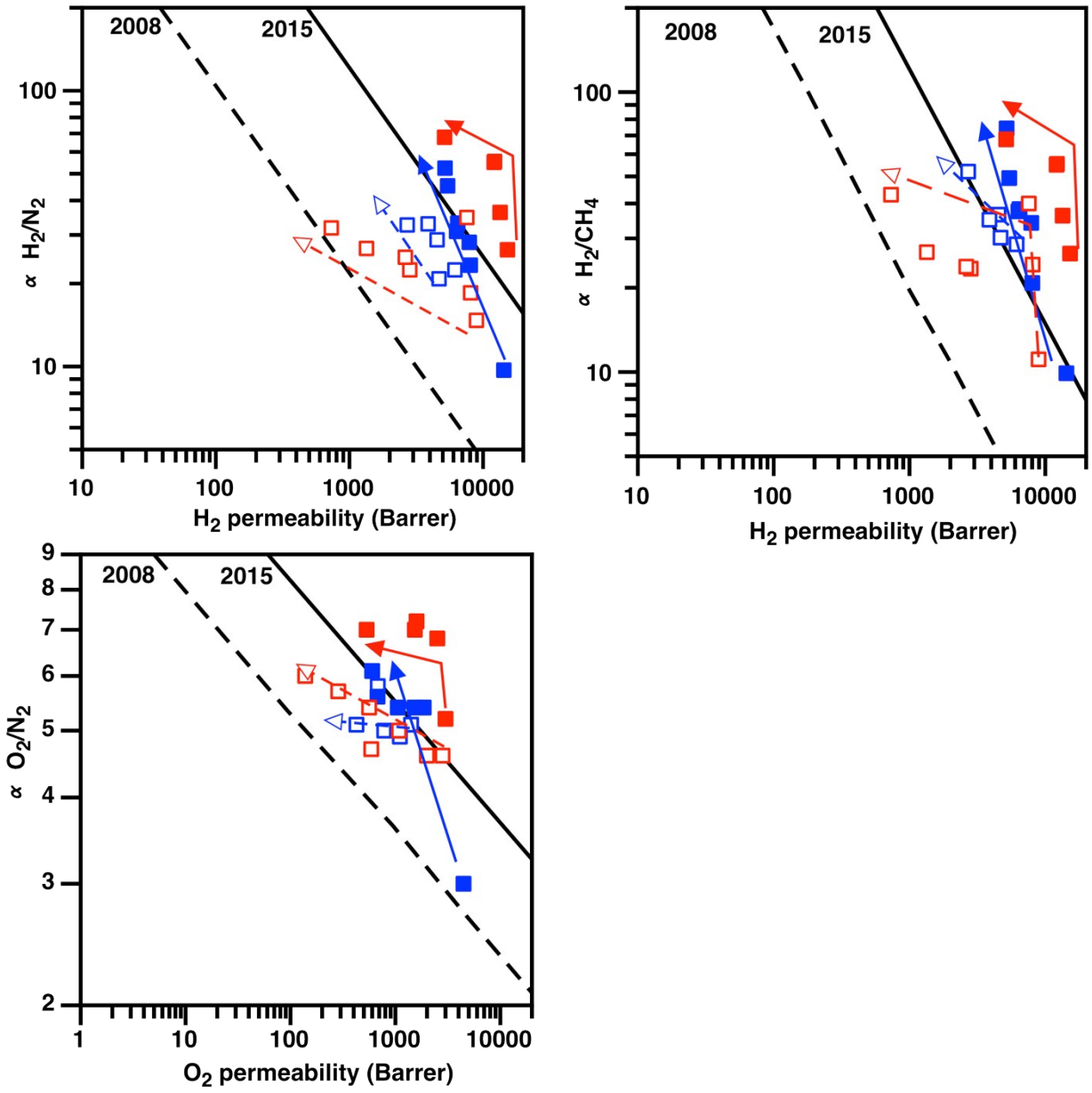

Figure S24 The H_2/N_2, H_2/CH_4 and O_2/N_2 separation performances of PIM-EA(Me_2)-TB/PAF-1 membranes remain beyond the 2015 upper bound.[9] Arrows indicate the 2-year long physical aging process. PIM- EA(Me_2)-TB (□), PIM- EA(Me_2)-TB/PAF-1 (■), PIM-EA(H_2)-TB (□), and PIM-EA(H_2)-TB/PAF-1 (■). These data were collected in the Hill Lab at CSIRO, Australia.

Single gas permeation data in Tables S5 – 8 were collected in CSIRO labs at 2 bar, 25 ˚C.

Table S5 Single gas permeabilities and selectivities for PIM-EA(H_2)-TB

Aging (Days)	Single gas permeability (Barrer)						Single gas selectivity		
	He	H_2	O_2	N_2	CH_4	CO_2	H_2/N_2	H_2/CH_4	O_2/N_2
0	1580	6150	1410	275	215	6660	22.4	28.6	5.1
7		4680	1100	225	155	3760	20.8	30.2	4.9
14		4530	782	157	124	2980	28.8	36.5	5.0
90	1270	3880	679	118	111	2300	32.9	35.0	5.8
730	1040	2710	425	83	52	1240	32.0	52.0	5.1

Table S6 Single gas permeabilities and selectivities for PIM-EA(H_2)-TB/PAF-1

Aging (Days)	Single gas permeability (Barrer)						Single gas selectivity		
	He	H_2	O_2	N_2	CH_4	CO_2	H_2/N_2	H_2/CH_4	O_2/N_2
0	6120	14310	4460	1480	1440	14120	9.7	9.9	3.0
7	4880	8020	1860	340	385	6340	23.3	20.8	5.4
30	-	7890	1530	280	230	6080	28.2	34.1	5.4
60	-	6460	1050	195	170	3440	33.1	38.2	5.4
90	-	6340	1030	205	170	3380	30.9	37.5	5.0
120	2300	5430	680	120	110	2470	45.2	49.3	5.6
730	2290	5190	600	99	70	1880	52.4	74.2	6.1

Table S7 Single gas permeabilities and selectivities for PIM-EA(Me_2)-TB

Aging (Days)	Single gas permeability (Barrer)						Single gas selectivity		
	He	H_2	O_2	N_2	CH_4	CO_2	H_2/N_2	H_2/CH_4	O_2/N_2
0	3040	8920	2810	608	804	8200	14.7	11.1	4.6
7	-	8070	1995	435	334	6980	18.5	24.2	4.6
14	-	7560	1080	218	189	5840	34.7	40.0	5.0
30	-	2830	588	126	121	2550	22.4	23.4	4.7
60	-	2620	562	105	110	2170	24.9	23.8	5.4
90	2210	1340	285	50	50	1320	26.8	26.8	5.7
730	310	731	138	23	17	504	31.8	43.0	6.0

Table S8 Single gas permeabilities and selectivities for PIM-EA(Me_2)-TB/PAF-1

Aging (Days)	Single gas permeability (Barrer)						Single gas selectivity		
	He	H_2	O_2	N_2	CH_4	CO_2	H_2/N_2	H_2/CH_4	O_2/N_2
0	4510	15230	3000	575	718	9780	26.5	21.2	5.2
7	-	13410	2510	371	312	9600	36.2	43.0	6.8
14	-	12190	1590	220	228	4380	55.4	53.4	7.2
90	4550	12110	1530	220	200	4350	55.0	60.5	7.0
730	2410	5150	531	76	54	1730	67.8	95.4	7.0

Table S9 Relative changes in single and mixed gas permeabilities of PAF-1 loaded membranes (aged 90 days) studied here as a function of gas (partial) pressures.

Samples (aged 90 days)	Partial pressure (atm)	Gas permeability (Barrer)					
		CO_2			CH_4		
		Single	Mixed	Δ %	Single	Mixed	Δ %
PIM-EA(Me_2)-TB/PAF-1	3	6329	7237	+14 %	833	1085	+30 %
	20	6191	6579	+7 %	837	1768	+111 %
PIM-EA(H_2)-TB/PAF-1	3	4429	4842	+9 %	286	511	+78 %
	20	3547	3670	+3 %	288	704	+144 %

S12. H_2/CH_4 separation performance at realistic operating conditions

The resulting high H_2 permeabilities and H_2/CH_4 selectivities of aged PIM-EA(Me_2)-TB/PAF-1 and PIM-EA(H_2)-TB/PAF-1 nanocomposites could be promising for recovering H_2 from the off-gas of hydrocracker refineries in high temperature and pressure conditions.[10] High operating pressures typically lead to gas-induced plasticisation[11] and high temperatures could mobilize polymer chains in membranes;[12] enhancing gas permeabilities while reducing gas selectivities. Requirements of polymer membranes for H_2 recovery include (1) ability to achieve H_2/CH_4 selectivities between 20 – 25,[13] (2) withstand gas-induced plasticisation[11] at operating pressures up to 20 bar and (3) retain polymer chain mobility between 60 – 200 ˚C[10] to maintain high gas permeabilities and selectivities.[12]

Using 50:50 H_2/CH_4 mixtures, the gas membrane performances of aged films and nanocomposites (90 days) were significantly lower than those of single gas separation (Table S10). This was due to the competitive processes between H_2 and CH_4 gas molecules for transportation pathways in mixtures.[14] Mixed gas H_2 permeability was reduced by 49 %, while CH4 permeability was enhanced by 41 %; leading to a 60 % reduction in H_2/CH_4 mixed gas selectivity, from 60.5 to 22. Even with a mixed gas selectivity of 22, aged PIM-EA(Me_2)-TB/PAF-1 membranes could produce 95 % purity H_2 from 50:50 H_2/ CH_4 mixtures; making them ideal as a stand-alone separation technology that could potentially enhance the energy efficiency of H_2 recovery from refineries. The lower mixed gas H_2/CH_4 selectivity of PIM-EA(H_2)-TB/PAF-1 nanocomposites would not produce H_2 of sufficient purity for recycling purposes in hydrocrackers.

Table S10 A comparison of the single gas and mixed gas H2 and CH4 permeabilities of samples aged for 90 days. Single gas permeation tests were carried out at 35 ˚C, 2 atm in the Ferrari Lab at UoE, while the mixed gas permeation tests were carried out at 35 ˚C, with 50:50 mol.% H_2:CH_4 at 35 ˚C in the Hill group at CSIRO.

Samples aged for 90 days	Type of gas permeation measurement	Gas permeability (Barrer)		H_2/CH_4 selectivity	H_2 purity (%)
		H_2	CH_4		
PIM-EA(H_2)-TB	Single	3880	111	35.0	97
	Mixed	1696	151	11.2	92
PIM-EA(H_2)-TB/PAF-1	Single	6340	170	37.5	97
	Mixed	5882	675	8.7	90
PIM-EA(Me_2)-TB	Single	1340	50	26.8	96
	Mixed	1319	119	11.1	92
PIM-EA(Me_2)-TB/PAF-1	Single	12110	200	60.5	98
	Mixed	6190	281	22	95

As hydrocracking reactors operate at 350 – 400 ˚C, the actual temperature of off-gas from refineries can be at much higher temperatures.[15] At 200 ˚C, 10 bar (conditions similar to mild hydrocracking process[16]), the H_2 permeability of aged (90 days) PIM-EA(Me_2)-TB/PAF-1 was retained at 9,000 Barrer; highlighting the suitability of these nanocomposite membranes for H_2 recovery in realistic operating conditions (Fig. S26). In the same operating conditions, the H_2 permeability of aged PIM-EA(H_2)-TB/PAF-1 nanocomposites was reduced by 25 %. This decrease in H_2 permeability was attributed to physical aging. More importantly, even after physical aging, the H_2/CH_4 separation performances of aged, thick PIM-EA(Me_2)-TB/PAF-1 films outperformed traditional materials for H_2 purification including polyimides, polysulfones, and cellulose acetate. This is of importance for the design of new modules where space and weight constraints will be increased.

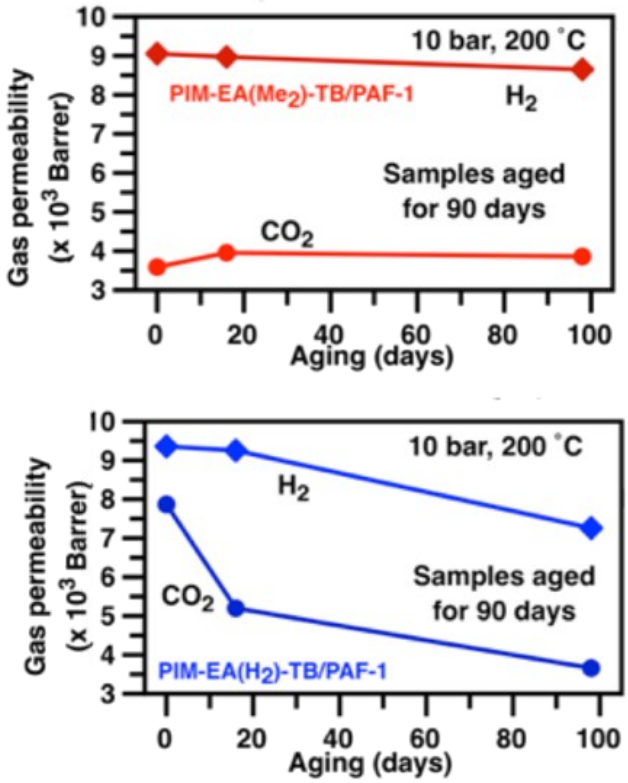

Figure S25 The single gas (H_2 – ◆, CO_2 – ●) separation performances of PIM-EA(Me_2)-TB/PAF-1 (red) and PIM-EA(H_2)-TB/PAF-1 (blue) at 10 bar and 200 °C.

S13. References

1 Cristol, S. J. & Hause, N. L. Mechanisms of elimination reactions. V. Preparation and elimination reactions of cis- and trans-11,12-dichloro-9,10-dihydro-9,10-ethanoanthracene. *J. Am. Chem. Soc.* **74**, 2193-2197, (1952).

2 Eldrup, M., Lightbody, D. & Sherwood, J. N. The temperature dependence of positron lifetimes in solid pivalic acid. *Chemical Physics* **63**, 51-58, (1981).

3 Tao, S. J. Positronium Annihilation in Molecular Substances. *The Journal of Chemical Physics* **56**, 5499-5510, (1972).

4 Dull, T. L., Frieze, W. E., Gidley, D. W., Sun, J. N. & Yee, A. F. Determination of Pore Size in Mesoporous Thin Films from the Annihilation Lifetime of Positronium. *The Journal of Physical Chemistry B* **105**, 4657-4662, (2001).

5 Hill, A. J. *et al.* Influence of methanol conditioning and physical aging on carbon spin-lattice relaxation times of poly(1-trimethylsilyl-1-propyne). *Journal of Membrane Science* **243**, 37-44, (2004).

6 Lau, C. H. *et al.* Gas-Separation Membranes Loaded with Porous Aromatic Frameworks that Improve with Age. *Angewandte Chemie International Edition* **54**, 2669-2673, (2015).

7 Lau, C. H. *et al.* Ending Aging in Super Glassy Polymer Membranes. *Angewandte Chemie International Edition* **53**, 5322-5326, (2014).

8 Gleason, K. L., Smith, Z. P., Liu, Q., Paul, D. R. & Freeman, B. D. Pure- and mixed-gas permeation of CO2 and CH4 in thermally rearranged polymers based on 3,3′-dihydroxy-4,4′-diamino-biphenyl (HAB) and 2,2′-bis-(3,4-dicarboxyphenyl) hexafluoropropane dianhydride (6FDA). *Journal of Membrane Science* **475**, 204-214, (2015).

9 Swaidan, R., Ghanem, B. & Pinnau, I. Fine-Tuned Intrinsically Ultramicroporous Polymers Redefine the Permeability/Selectivity Upper Bounds of Membrane-Based Air and Hydrogen Separations. *ACS Macro Letters* **4**, 947-951, (2015).

10 Baker, R. W. Future Directions of Membrane Gas Separation Technology. *Industrial & Engineering Chemistry Research* **41**, 1393-1411, (2002).

11 Tiwari, R. R., Jin, J., Freeman, B. D. & Paul, D. R. Physical aging, CO_2 sorption and plasticization in thin films of polymer with intrinsic microporosity (PIM-1). *Journal of Membrane Science* **537**, 362-371, (2017).

12 Peramanu, S., Cox, B. G. & Pruden, B. B. Economics of hydrogen recovery processes for the purification of hydroprocessor purge and off-gases. *International Journal of Hydrogen Energy* **24**, 405-424, (1999).

13 Sanders, D. F. *et al.* Energy-efficient polymeric gas separation membranes for a sustainable future: A review. *Polymer* **54**, 4729-4761, (2013).

14 Tanaka, K., Taguchi, A., Hao, J., Kita, H. & Okamoto, K. Permeation and separation properties of polyimide membranes to olefins and paraffins. *Journal of Membrane Science* **121**, 197-207, (1996).

15 Kaldis, S. P., Kapantaidakis, G. C. & Sakellaropoulos, G. P. Simulation of multicomponent gas separation in a hollow fiber membrane by orthogonal collocation — hydrogen recovery from refinery gases. *Journal of Membrane Science* **173**, 61-71, (2000).

16 Speight, J. G. New approaches to hydroprocessing. *Catalysis Today* **98**, 55-60, (2004).